PHYSICAL REVIEW C **94**, 045206 (2016)

# Measurement of target and double-spin asymmetries for the $\vec{e}\vec{p} \rightarrow e\pi^+(n)$ reaction in the nucleon resonance region at low $Q^2$

X. Zheng,[1] K. P. Adhikari,[2,3] P. Bosted,[4] A. Deur,[4,1] V. Drozdov,[5,6] L. El Fassi,[2,7] Hyekoo Kang,[8] K. Kovacs,[1] S. Kuhn,[3]
E. Long,[9] S. K. Phillips,[9] M. Ripani,[5] K. Slifer,[9] L. C. Smith,[1] D. Adikaram,[3,*] Z. Akbar,[10] M. J. Amaryan,[3]
S. Anefalos Pereira,[11] G. Asryan,[12] H. Avakian,[4] R. A. Badui,[13] J. Ball,[14] N. A. Baltzell,[4,15] M. Battaglieri,[5] V. Batourine,[4]
I. Bedlinskiy,[16] A. S. Biselli,[17,18] W. J. Briscoe,[19] S. Bültmann,[3] V. D. Burkert,[4] D. S. Carman,[4] A. Celentano,[5] S. Chandavar,[20]
G. Charles,[21] J.-P. Chen,[4] T. Chetry,[20] Seonho Choi,[8] G. Ciullo,[22] L. Clark,[23] L. Colaneri,[24,25] P. L. Cole,[26] N. Compton,[20]
M. Contalbrigo,[22] V. Crede,[10] A. D'Angelo,[24,25] N. Dashyan,[12] R. De Vita,[5] E. De Sanctis,[11] C. Djalali,[15] G. E. Dodge,[3]
R. Dupre,[21] H. Egiyan,[4,9] A. El Alaoui,[27] L. Elouadrhiri,[4] P. Eugenio,[10] E. Fanchini,[5] G. Fedotov,[15,6] R. Fersch,[28] A. Filippi,[29]
J. A. Fleming,[30] N. Gevorgyan,[12] Y. Ghandilyan,[12] G. P. Gilfoyle,[31] K. L. Giovanetti,[32] F. X. Girod,[4,14] C. Gleason,[15]
E. Golovach,[6] R. W. Gothe,[15] K. A. Griffioen,[33] M. Guidal,[21] N. Guler,[3,†] L. Guo,[13,4] C. Hanretty,[1,*] N. Harrison,[4]
M. Hattawy,[7] K. Hicks,[20] M. Holtrop,[9] S. M. Hughes,[30] Y. Ilieva,[15,19] D. G. Ireland,[23] B. S. Ishkhanov,[6] E. L. Isupov,[6]
D. Jenkins,[34] H. Jiang,[15] H. S. Jo,[21] S. Joosten,[35] D. Keller,[1] G. Khachatryan,[12] M. Khandaker,[26,36] A. Kim,[37] W. Kim,[38]
F. J. Klein,[39] V. Kubarovsky,[4,40] L. Lanza,[24,25] P. Lenisa,[22] K. Livingston,[23] I. J. D. MacGregor,[23] N. Markov,[37]
B. McKinnon,[23] M. Mirazita,[11] V. Mokeev,[4,6] A. Movsisyan,[22] E. Munevar,[4,19] C. Munoz Camacho,[21] G. Murdoch,[23]
P. Nadel-Turonski,[4,39] L. A. Net,[15] A. Ni,[38] S. Niccolai,[21] G. Niculescu,[32] I. Niculescu,[32] M. Osipenko,[5] A. I. Ostrovidov,[10]
M. Paolone,[35] R. Paremuzyan,[9] K. Park,[4,38] E. Pasyuk,[4] P. Peng,[1] S. Pisano,[11] O. Pogorelko,[16] J. W. Price,[41] A. J. R. Puckett,[37]
B. A. Raue,[13,4] A. Rizzo,[24,25] G. Rosner,[23] P. Rossi,[4,11] P. Roy,[10] F. Sabatié,[14] C. Salgado,[36] R. A. Schumacher,[18]
Y. G. Sharabian,[4] Iu. Skorodumina,[15,6] G. D. Smith,[30] D. Sokhan,[23] N. Sparveris,[35] I. Stankovic,[30] I. I. Strakovsky,[19]
S. Strauch,[15,19] M. Taiuti,[5,42] Ye Tian,[15] M. Ungaro,[4,37] H. Voskanyan,[12] E. Voutier,[21] N. K. Walford,[39] D. P. Watts,[30] X. Wei,[4]
L. B. Weinstein,[3] M. H. Wood,[43,15] N. Zachariou,[30] J. Zhang,[4] and I. Zonta[24,25]
(CLAS Collaboration)
[1]*University of Virginia, Charlottesville, Virginia 22901, USA*
[2]*Mississippi State University, Mississippi State, Mississippi 39762, USA*
[3]*Old Dominion University, Norfolk, Virginia 23529, USA*
[4]*Thomas Jefferson National Accelerator Facility, Newport News, Virginia 23606, USA*
[5]*INFN, Sezione di Genova, I-16146 Genova, Italy*
[6]*Skobeltsyn Institute of Nuclear Physics, Lomonosov Moscow State University, 119234 Moscow, Russia*
[7]*Argonne National Laboratory, Argonne, Illinois 60439, USA*
[8]*Seoul National University, Seoul, Korea*
[9]*University of New Hampshire, Durham, New Hampshire 03824, USA*
[10]*Florida State University, Tallahassee, Florida 32306, USA*
[11]*INFN, Laboratori Nazionali di Frascati, I-00044 Frascati, Italy*
[12]*Yerevan Physics Institute, 375036 Yerevan, Armenia*
[13]*Florida International University, Miami, Florida 33199, USA*
[14]*CEA, Centre de Saclay, Irfu/Service de Physique Nucléaire, F-91191 Gif-sur-Yvette, France*
[15]*University of South Carolina, Columbia, South Carolina 29208, USA*
[16]*Institute of Theoretical and Experimental Physics, Moscow, 117259, Russia*
[17]*Fairfield University, Fairfield, Connecticut 06824, USA*
[18]*Carnegie Mellon University, Pittsburgh, Pennsylvania 15213, USA*
[19]*The George Washington University, Washington, DC 20052, USA*
[20]*Ohio University, Athens, Ohio 5701, USA*
[21]*Institut de Physique Nucléaire, CNRS/IN2P3 and Université Paris Sud, F-Orsay, France*
[22]*INFN, Sezione di Ferrara, I-44100 Ferrara, Italy, USA*
[23]*University of Glasgow, Glasgow G12 8QQ, United Kingdom*
[24]*INFN, Sezione di Roma Tor Vergata, I-00133 Rome, Italy*
[25]*Universita' di Roma Tor Vergata, I-00133 Rome, Italy*
[26]*Idaho State University, Pocatello, Idaho 83209, USA*
[27]*Universidad Técnica Federico Santa María, Casilla 110-V Valparaíso, Chile*
[28]*Christopher Newport University, Newport News, Virginia 23606, USA*
[29]*INFN, Sezione di Torino, I-10125 Torino, Italy*
[30]*Edinburgh University, Edinburgh EH9 3JZ, United Kingdom*
[31]*University of Richmond, Richmond, Virginia 23173, USA*
[32]*James Madison University, Harrisonburg, Virginia 22807, USA*
[33]*College of William and Mary, Williamsburg, Virginia 23187, USA*
[34]*Virginia Tech, Blacksburg, Virginia 24061, USA*
[35]*Temple University, Philadelphia, Pennsylvania 19122, USA*

2469-9985/2016/94(4)/045206(19)

[36]*Norfolk State University, Norfolk, Virginia 23504, USA*
[37]*University of Connecticut, Storrs, Connecticut 06269, USA*
[38]*Kyungpook National University, Daegu 702-701, Republic of Korea*
[39]*Catholic University of America, Washington, DC 20064, USA*
[40]*Rensselaer Polytechnic Institute, Troy, New York 12180, USA*
[41]*California State University, Dominguez Hills, Carson, California 90747, USA*
[42]*Università di Genova, Dipartimento di Fisica, 16146 Genova, Italy*
[43]*Canisius College, Buffalo, New York 14208, USA*

(Received 13 July 2016; published 19 October 2016)

We report measurements of target- and double-spin asymmetries for the exclusive channel $\vec{e}\vec{p} \to e\pi^+(n)$ in the nucleon resonance region at Jefferson Lab using the CEBAF Large Acceptance Spectrometer (CLAS). These asymmetries were extracted from data obtained using a longitudinally polarized $NH_3$ target and a longitudinally polarized electron beam with energies 1.1, 1.3, 2.0, 2.3, and 3.0 GeV. The new results are consistent with previous CLAS publications but are extended to a low $Q^2$ range from 0.0065 to 0.35 $(\mathrm{GeV}/c)^2$. The $Q^2$ access was made possible by a custom-built Cherenkov detector that allowed the detection of electrons for scattering angles as low as 6°. These results are compared with the unitary isobar models JANR and MAID, the partial-wave analysis prediction from SAID, and the dynamic model DMT. In many kinematic regions our results, in particular results on the target asymmetry, help to constrain the polarization-dependent components of these models.

DOI: 10.1103/PhysRevC.94.045206

## I. PHYSICS MOTIVATION

The perturbative nature of the strong interaction at small distances—often referred to as "asymptotic freedom"—was established more than 30 years ago and provided strong support for quantum chromodynamics (QCD) to be accepted as the correct theory for strong interactions [1,2]. On the other hand, calculations at long distances are still beyond reach because of the nonperturbative nature at this scale. As a result, we are still far away from being able to describe the strong force as it manifests itself in the structure of baryons and mesons [3,4]. A fundamental approach to resolve this difficulty is to develop accurate numerical simulations of QCD on the lattice; for recent reviews see [5,6]. However lattice QCD methods are difficult to apply to light-quark systems such as the nucleon. Alternatively, hadron models with effective degrees of freedom have been constructed to interpret data. One example is the chiral perturbation theory [7,8], which is constrained only by the symmetry properties of QCD. The constituent quark model, though not fully understood, is one successful example that works almost everywhere from hadron spectroscopy to deep inelastic scattering [9,10]. Predictions for the scattering amplitudes and polarization-dependent asymmetries exist for many resonances within the framework of the relativistic constituent quark model (RCQM) [11] and the single quark transition model (SQTM) [12].

The comparison between these predictions and experimental results, on the other hand, is not straightforward. This is because the experimentally measured cross sections and asymmetries are usually complicated combinations of resonant and nonresonant amplitudes and couplings, and their interference terms. To compare with theories, partial wave analyses are often used to extract these amplitudes and resonance couplings from data. Once comparisons can be made, data are used to provide inputs for constructing or adjusting meson production mechanisms in theories and models, such as proper treatment of the hadronic final state and implementation of the nonresonant part of the meson production amplitude. These mechanisms are usually not included in quark models. Examples of phenomenological partial wave analyses that can benefit from more data are MAID [13], JANR [14], SAID [15], and the DMT [16] models. Electron-scattering data used to test these calculations include primarily $N - N^*$ transition form factors and response functions for meson production reactions obtained from Jefferson Lab (JLab), MAMI, and MIT-Bates. Recently, polarization observables such as double-spin asymmetries and target spin asymmetries for pion electroproduction from the proton have made the beam- and target-helicity response functions accessible [17–20], providing a new approach to testing models and to a greater understanding of the baryon resonance structure. As an example, the MAID model was based mostly on unpolarized data and is only recently being tested extensively against double polarization asymmetries. In general, polarization observables provide an important constraint on the understanding of the underlying helicity response functions or interference terms in $N \to \Delta$ and $N \to N^*$ resonances.

Compared to the proton, existing data on neutron excitation were particularly sparse. Neutron data have recently become available from JLab [21,22], which make it possible to test the isospin structure of models such as RCQM and SQTM. The neutron data will be valuable to the development of many phenomenological analyses as well because they need to incorporate double polarization asymmetry data for all pion production channels from both the proton and the neutron to perform the full isospin decomposition.

In addition, data at very low $Q^2$ values are often desired for testing the chiral perturbation theory and to study the transition

---

[*] Present address: Thomas Jefferson National Accelerator Facility, Newport News, Virginia 23606, USA.

[†] Present address: Los Alamos National Laboratory, Los Alamos, New Mexico 87544, USA.

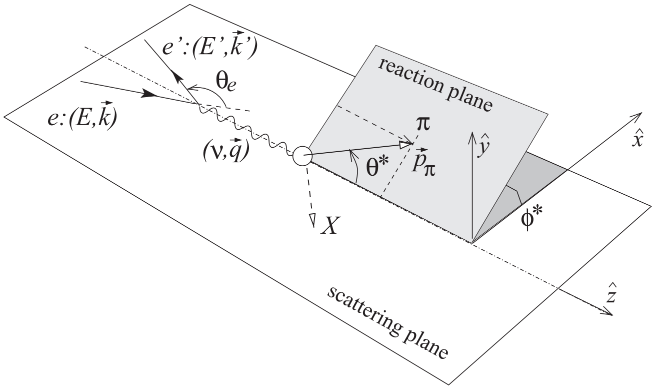

FIG. 1. Kinematics of single pion electroproduction. The Lorentz boost associated with the transformation from the laboratory to the CM frame of the $\gamma^*N$ system is along the momentum transfer $\vec{q}$, where the coordinates $\hat{x},\hat{y},\hat{z}$ of the CM frame are defined in this picture.

from virtual photons to the real photon point ($Q^2 = 0$). Here, $Q^2$ is defined as $Q^2 \equiv -q^2$, where $q \equiv (\nu,\vec{q})$ is the four-momentum transferred from the incident electron to the target and

$$\nu \equiv E - E', \tag{1}$$

with $E$ and $E'$ the incident and the scattered electron's energies, respectively. At low energy transfers $\nu < 2$ GeV the most prominent resonances are the $\Delta(1232)3/2^+$,$N(1520)3/2^-$, and $N(1680)5/2^+$ [11]. For the $N(1520)3/2^-$ and $N(1680)5/2^+$, their amplitudes at large $Q^2$ are determined by perturbative QCD and hadron helicity conservation. It is expected in this region that $A^N \to 1$, where $A^N$ is the virtual photon helicity asymmetry defined as

$$A^N = \frac{|A_{1/2}|^2 - |A_{3/2}|^2}{|A_{1/2}|^2 + |A_{3/2}|^2}, \tag{2}$$

with $A_{1/2,3/2}$ the scattering amplitudes and the subscripts indicate the total spin projection of the virtual photon and the nucleon target along the virtual photon's momentum. However, data using real photons show a strong helicity-3/2 dominance and $A^N \to -1$ [23]. This indicates that $A^N$ for these two resonances must cross zero at some intermediate $Q^2$ and there have been calculations for the $Q^2$ dependence of $A^N$ from various models [11,12,24]. For pion electroproduction, the double-spin asymmetry is dominated by $A^N$ [17] and thus data on this observable will allow us to test a possible sign flip for the $N(1520)3/2^-$ and $N(1680)5/2^+$ resonances. Data on the double-spin asymmetry of pion photoproduction have recently become available from the CBELSA/TAPS Collaboration [25] and are also expected from JLab experiments [26–28]; all used the frozen spin target with a longitudinal polarization and a circularly polarized photon beam. These photoproduction data will further test the transition to the real photon point.

### A. Formalism for pion electroproduction

Figure 1 shows the kinematics of single pion production in the Born approximation: The electron transfers a virtual photon $\gamma^*$ of four-momentum $q \equiv (\nu,\vec{q})$ to the target nucleon $N$ which forms a nucleon resonance. The resonance then decays into a pion and another particle $X$. Two planes are used to describe this process: the scattering (leptonic) plane defined by the incoming and outgoing electrons' momenta $\vec{k}$ and $\vec{k}'$, and the reaction (hadronic) plane defined by the momentum of the virtual photon $\vec{q}$ and the momentum of the outgoing pion $\vec{p}_\pi$.

The reaction is usually described in terms of $Q^2$, the invariant mass $W$ of the $\gamma^*N$ system (which is also the $\pi X$ system), and two angles $\theta^*$ and $\phi^*$. Here, $\theta^*$ is the angle formed by $\vec{q}$ and $\vec{p}_\pi$, and $\phi^*$ is the angle formed by rotating the leptonic plane to the hadronic plane. If one defines the $\gamma^*N$ center-of-mass (CM) frame with $\hat{z}$ pointing along $\vec{q}$,$\hat{y}$ along $\vec{q} \times \vec{k}$, then $\theta^*$ and $\phi^*$ are the polar and the azimuthal angles of the emitted pion. The energy transfer is related to $Q^2$ and $W$ via

$$\nu = \frac{W^2 + Q^2 - M^2}{2M}, \tag{3}$$

with $M$ the nucleon mass. The differential cross section for the reaction $\vec{e}\vec{N} \to e\pi(X)$ with longitudinally polarized beam and target can be written in the following form:

$$\frac{d^5\sigma_h}{dE_{e'}d\Omega_{e'}d\Omega^*_\pi} = \Gamma\frac{d\sigma_h}{d\Omega^*_\pi}, \tag{4}$$

with

$$\frac{d\sigma_h}{d\Omega^*_\pi} = \frac{d\sigma_0}{d\Omega^*_\pi} + P_b\frac{d\sigma_e}{d\Omega^*_\pi} + P_t\frac{d\sigma_t}{d\Omega^*_\pi} + P_bP_t\frac{d\sigma_{et}}{d\Omega^*_\pi}, \tag{5}$$

where $P_b$ and $P_t$ are, respectively, the polarizations of the electron beam and the target along the beam direction, $\sigma_0$ is the unpolarized cross section, and $\sigma_e$,$\sigma_t$, and $\sigma_{et}$ are the polarized cross-section terms when beam, target, and both beam and target are polarized. Note that the differential cross sections on the right-hand side of Eq. (5) are defined in the CM frame of the $\gamma^*N$ system, as indicated by the asterisk in the pion's solid angle. The virtual photon flux is

$$\Gamma = \frac{\alpha k_\gamma^{\rm lab}}{2\pi^2Q^2}\frac{E'}{E}\frac{1}{1-\epsilon}, \tag{6}$$

where $\alpha$ is the electromagnetic coupling constant, $k_\gamma^{\rm lab} = (W^2 - M^2)/2M$ is the photon equivalent energy in the laboratory frame, i.e., the energy needed by a real photon to excite the nucleon to an invariant mass $W$. The virtual photon polarization is given by

$$\epsilon = \left[1 + \frac{2|\vec{q}|^2}{Q^2}\tan^2\frac{\theta_e}{2}\right]^{-1}, \tag{7}$$

where $\theta_e$ is the angle between the incident and outgoing electrons in the laboratory frame. The $Q^2$ can be calculated as

$$Q^2 = 4EE'\sin^2\frac{\theta_e}{2}. \tag{8}$$

To evaluate the pion's kinematics in the CM frame of the $\gamma^*N$ system, we relate a laboratory-frame 4-momentum vector $p^\mu$ to the CM frame $p^\mu_{\rm cm}$ via a Lorentz boost with $\vec{\beta} = \hat{z}|\vec{q}|/(\nu + M)$ and $\gamma = (\nu + M)/W$:

$$p^0_{\rm cm} = \gamma p^0 - \gamma\beta p^z, \tag{9}$$

$$p^x_{\rm cm} = p^x, \tag{10}$$

$$p^y_{\rm cm} = p^y, \tag{11}$$

$$p^z_{\rm cm} = -\gamma\beta p^0 + \gamma p^z. \tag{12}$$

Specifically, we have for the virtual photon:

$$|\vec{q}_{\rm cm}| = \frac{M}{W}|\vec{q}|, \tag{13}$$

$$\nu_{\rm cm} = \frac{\nu M - Q^2}{W}. \tag{14}$$

For the pion,

$$E_{{\rm cm},\pi} = \gamma(E_\pi - \beta|\vec{p}_\pi|\cos\theta_\pi), \tag{15}$$

$$p_{z,{\rm cm},\pi} = \gamma(|\vec{p}_\pi|\cos\theta_\pi - \beta E_\pi), \tag{16}$$

where $\theta_\pi = \arccos[(\vec{q}\cdot\vec{p}_\pi)/(|\vec{q}||\vec{p}_\pi|)]$ is the angle between the pion momentum and $\vec{q}$ in the laboratory frame, and $E_\pi$ is the pion energy again in the laboratory frame. The polar angle of the pion in the CM frame is given by

$$\theta^* = \arccos\left[\frac{p_{z,{\rm cm},\pi}}{\sqrt{E_{{\rm cm},\pi} - m_\pi^2}}\right], \tag{17}$$

where $m_\pi$ is the pion mass. The azimuthal angle of the pion is the same in the laboratory and the CM frame, given by

$$\phi^* = \arccos\left[\frac{\vec{a}\cdot\vec{b}}{|\vec{a}||\vec{b}|}\right], \tag{18}$$

with $\vec{a} \equiv \vec{q} \times \vec{k}$ and $\vec{b} \equiv \vec{q} \times \vec{p}_\pi$. In this paper, the range of $\phi^*$ is defined from 0 to $2\pi$, i.e., a shift of $2\pi$ is added to $\phi^*$ if the result from Eq. (18) is negative.

The beam, target, and double beam-target asymmetries are

$$A_{LU} = \frac{\sigma_e}{\sigma_0}, \tag{19}$$

$$A_{UL} = \frac{\sigma_t}{\sigma_0}, \tag{20}$$

$$A_{LL} = -\frac{\sigma_{et}}{\sigma_0}, \tag{21}$$

where each cross section $\sigma$ stands for the $d\sigma/d\Omega^*_\pi$ of Eq. (5). Note that we have adopted an extra minus sign in the definition of $A_{LL}$ to be consistent with Eq. (2) and previous CLAS publications [17–19].

In this paper, we report on results of both $A_{UL}$ and $A_{LL}$ extracted from the JLab CLAS EG4 [29,30] data. The beam asymmetry $A_{LU}$ was also extracted from the data, but was used only as a cross check of the beam helicity and is not presented here. These results are available for download from the CLAS database.

### B. Previous data

The first double-spin asymmetry for the $\pi^+ n$ channel was published based on the CLAS EG1a data with a 2.6-GeV beam, for a $Q^2$ range from 0.35 to 1.5 (GeV/$c$)$^2$ [17,18]. The $\vec{e}\vec{p} \to e'p(\pi^0)$ channel was analyzed for the $\Delta(1232)3/2^+$ region using the same data set [19]. Similar analysis using the CLAS EG1b data was completed [20,22], in which the target and the double-spin asymmetries were extracted from both the $\vec{e}\vec{p} \to e'\pi^+(n)$ and $\vec{e}\vec{n} \to e'\pi^- p$ channels using 1.6–5.7 GeV beams with $Q^2$ as low as 0.1 (GeV/$c$)$^2$.

## II. THE JLAB CLAS EG4 EXPERIMENT

The main physics goal of the CLAS EG4 experiment [29,30] was to measure the inclusive spin structure functions on the proton and the deuteron, and to extract the generalized Gerasimov-Drell-Hearn (GDH) sum near the photon point. The original GDH sum rule [31,32], defined for real photons, is a fundamental prediction on the nucleon's spin structure that relates the helicity-dependent total photoabsorption cross section to the nucleon anomalous magnetic moment. The definition of the GDH sum was generalized to virtual photons [33,34], and the value of the generalized GDH sum at low $Q^2$ was predicted in the chiral perturbation theory. Similar to the pion production results presented here, the goal of the EG4's inclusive analysis is to test the chiral perturbation theory prediction and to compare the extrapolation to the $Q^2 = 0$ point with the GDH sum rule of the real photon.

The experiment was carried out in 2006 in experimental Hall B of JLab. Inclusive data were collected in the range $1 < W < 2$ GeV/$c^2$ and $Q^2$ down to 0.015 (GeV/$c$)$^2$ [35], using six beam energies (1.1, 1.3, 1.5, 2.0, 2.3, 3.0 GeV) on a polarized NH$_3$ target and two energies (1.3, 2.0 GeV) on a polarized ND$_3$ target. The average polarizations of NH$_3$ and ND$_3$ typically ranged within 75%–90% and 30%–45%, respectively. For the exclusive channel, only NH$_3$ data with beam energies of 1.1, 1.3, 2.0, 2.3, and 3.0 GeV were analyzed with the lowest $Q^2$ being 0.0065 (GeV/$c$)$^2$. The 1.5-GeV energy data were excluded because they were taken for run commissioning purposes and had limited statistics. For ND$_3$ data, the target spin direction was not flipped during the run, which makes it impossible to extract $A_{UL}$ or the complete information on $A_{LL}$ from the exclusive channel.

### A. The CLAS detector

The CEBAF Large Acceptance Spectrometer (CLAS) was used to detect scattered particles [36]. Figure 2 shows the basic structure of CLAS during EG4 with the polarized target installed. CLAS is an almost hermetic detector, optimized for the measurement of multiparticle final states in a large momentum region. The detector design is based on a toroidal magnet made by six superconducting coils arranged around the beam line to produce a field pointing primarily in the azimuthal direction. The field direction can be set such that the scattered negatively charged particles can be either bent away from the beamline ("electron outbending") or towards it ("electron inbending"). The detector itself is composed of six independent magnetic spectrometers, referred to as six "sectors," with a common target, trigger, and data acquisition system. Each sector is equipped with a three-layer drift chamber (DC) system for momentum and tracking determination, a time-of-flight (TOF) counter, a Cherenkov counter (CC), and a double-layer electromagnetic calorimeter (EC). The TOF, CC, and EC systems are primarily used for determining the particle type.

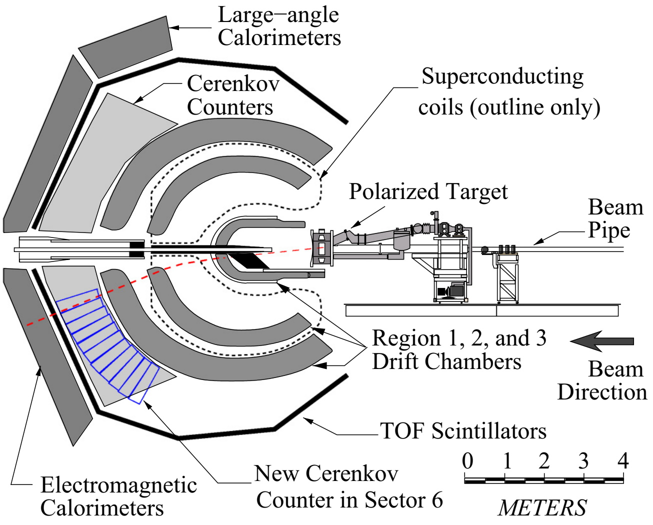

FIG. 2. CLAS during EG4 showing the polarized target and the detector arrangement. A new Cherenkov detector consisting of 11 segments was installed in place of the original Cherenkov in sector 6. It provided the ability of detecting scattered electrons in the outbending configuration with scattering angles as small as 6° (dashed-line track).

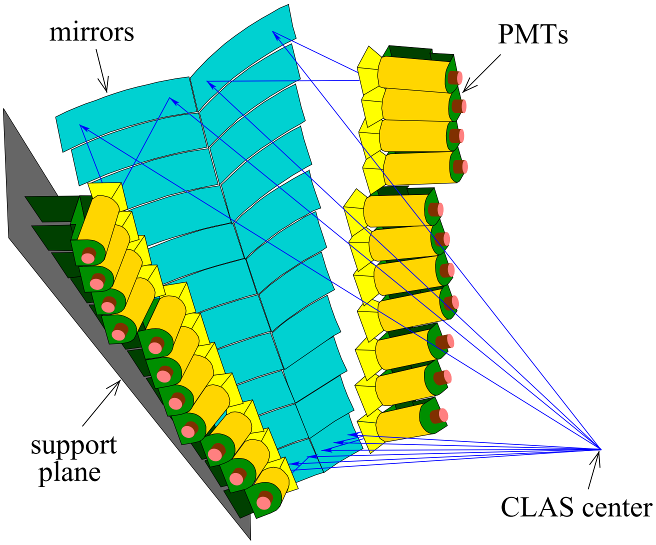

FIG. 3. The new Cherenkov detector designed and built by the INFN-Genova group. It consists of 11 pairs of mirrors with spherical curvature, which reflect the Cherenkov light to corresponding photomultiplier tubes (PMTs). Only one of the two support planes for the PMTs is shown here. The solid blue lines show simulated particle trajectories originated from the CLAS center and the reflection of the Cherenkov light towards the PMT.

To reach very low $Q^2$ while retaining the high beam energy needed to measure the GDH sum, a small scattering angle was necessary. This was achieved by running the CLAS torus magnet in the electron-outbending configuration. Although the standard CLAS Cherenkov detector geometrically reaches an 8° scattering angle [37], its structure is not ideal for collecting the Cherenkov light for outbending electrons. Therefore, for the EG4 experiment, a new Cherenkov detector was built by the INFN-Genova group and installed in sector 6, as shown in Fig. 2. It was designed to reach 6° scattering angle by optimizing the light collection for the electron-outbending configuration. Because of the very high counting rates at such low scattering angles, instrumenting only one CLAS sector was sufficient for the experiment. The new Cherenkov detector used the same radiator gas ($C_4F_{10}$) and the gas flow control system used in the standard CLAS Cherenkov. It consisted of 11 segments, each equipped with a pair of light-weight spherical mirrors; see Fig. 3. The mirrors were constructed following [38], by shaping a plexiglass layer onto a spherical mould, then gluing onto it a sandwich of carbon fiber and honeycomb, and finally evaporating a thin layer of aluminum onto the plexiglass. Each mirror reflected the light towards a light collector made of two pieces, an entrance section with the approximate shape of a truncated pyramid and a guiding section cylindrical in shape such as to match the circular photocathode. Each light collector was made of plexiglass with aluminum evaporated on the internal surface. The entrance section was built by a no-contact technique, where the plexiglass sheet was heated and pushed against a mould with the desired shape, then the bottom of the obtained object was cut to permit the free passage of light. The cylindrical section was obtained by cutting a plexiglass tube. The two sections were then glued together before evaporating the reflective layer. For the PMTs, the Photonis XP4508B with quartz window were chosen. The photoelectron yield was greater than $\approx 10$ within the kinematic region of the experiment, thereby yielding a high electron detection efficiency down to a scattering angle of about 6°. Signals from the new Cherenkov were built into the main electron trigger during EG4. Consequently only $1/6$ of the full azimuthal acceptance of CLAS was used to detect and identify forward-angle scattered electrons.

### B. The polarized electron beam

The polarized electron beam was produced by illuminating a strained GaAs photocathode with circularly polarized light. The helicity of the electron beam was selected from a pseudorandom sequence, and followed a quartet structure of either "$+--+$" or "$-++-$," with each helicity state lasting 33 ms. The helicity sequence controlled the trigger system, and periods of beam instability from helicity reversal were rejected from the data stream. To reduce possible systematic uncertainties, data were taken for two different beam helicity configurations, with the beam insertable half-wave plate (IHWP) inserted (in) and removed (out), respectively. The polarization of the electron beam was measured by both a Møller and a Mott polarimeter.

### C. The polarized targets

The polarized targets used for EG4 were the frozen $^{15}NH_3$ and $^{14}ND_3$ targets dynamically polarized at 1 K with a 5-Tesla field. These were the same as the targets used for previous CLAS double-polarization measurements [39]. The target material was irradiated with 20-MeV electrons prior to the

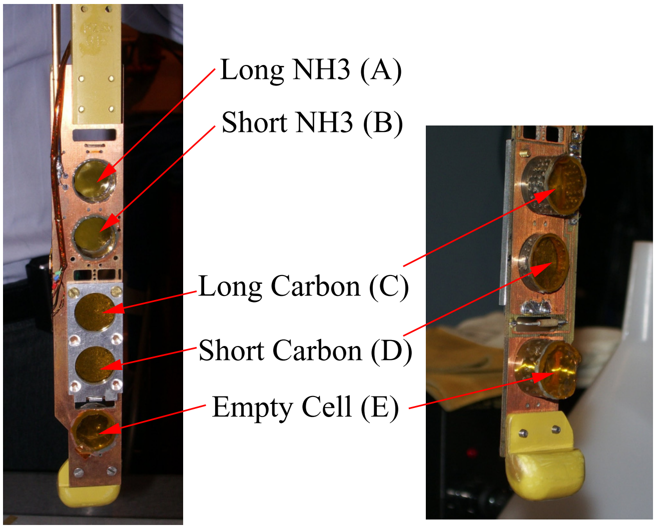

FIG. 4. Target insert used during the EG4 experiment. A 1.0-cm-long $NH_3$ and the 0.5-cm-long $NH_3$ targets were installed in the Long and Short $NH_3$ positions during the first half of the $NH_3$ run period. They were called the "long $NH_3$ top" and the "short $NH_3$" targets, respectively. During the second half of the $NH_3$ run, two 1.0-cm-long $NH_3$ targets were installed in the Long and the Short positions; they were called the "long $NH_3$ top" and the "long $NH_3$ bottom" targets, respectively. For the $ND_3$ run period only one 1.0-cm-long $ND_3$ target was installed in the Short position. The five target positions are labeled A, B, C, D, and E, as shown.

experiment to impart the paramagnetic radicals necessary for dynamic polarization. It was subsequently stored in liquid nitrogen ($LN_2$) until needed for the experiment. The material, in the form of 1–2-mm sized granules, was then removed from the $LN_2$ storage dewars and loaded into two cylindrical containers on the target insert. The structure of the target insert is shown in Fig. 4. The containers were either 1.0 cm or 0.5 cm in length, hereafter referred to as the long and short cells, respectively. The insert was then quickly placed into the target "banjo," a 1–2 liter vessel of 1-K liquid helium at the center of a 5-T superconducting split coil magnet. A complete description of the polarized target can be found in Ref. [40].

Because of the presence of gaps between the frozen crystals inside the target cell, even if the length of the target cell or the banjo could be determined precisely, the exact amount of polarized materials interacting with the electron beam could not be directly measured. The fraction of the target filled by frozen polarized material is called the "packing factor" and is typically extracted by comparing the yield from the polarized target to those from carbon and "empty" targets. For the carbon target, a carbon foil with known thickness was placed in an empty target cell and filled with liquid $^4$He. There were two carbon targets, labeled "long" and "short" carbon, of which both the cell length and the foil thickness match those of the long and the short $NH_3$ targets, respectively. Empty targets refer to target cells with no solid material inside. Empty targets can either be filled with liquid $^4$He, or the $^4$He can be completely pumped out. There was only one empty cell during EG4 to physically host the empty targets, which was 1.0 cm in length.

TABLE I. Targets used during EG4 along with their target lengths and densities. The target ID was the value recorded in the data. ID 10 was not used. The target position refers to the physical location on the target insert defined in Fig. 4.

| Target ID | Target type | Target position | length (cm) | Density (g/cm$^3$) |
|---|---|---|---|---|
| 1 | Long $NH_3$ top | A | 1.0 | 0.917[a] |
| 2 | Long $ND_3$ | B | 1.0 | 1.056[a] |
| 3 | Empty cell with helium | E | 1.0 | 0.145[b] |
| 4 | Long carbon | C | 1.0, 0.216[c] | 2.166[d] |
| 5 | Short $NH_3$ | B | 0.5 | 0.917[a] |
| 6 | Short carbon | D | 0.5, 0.108[c] | 2.166[d] |
| 7 | Long carbon no helium | C | 1.0, 0.216[c] | 2.166[d] |
| 8 | Empty cell without helium | E | 1.0 | |
| 9 | Short carbon without helium | D | 0.5 | 2.166[c] |
| 11 | Long $NH_3$ bottom | B | 1.0 | 0.917[a] |

[a] For polarized $NH_3$ or $ND_3$ the densities are the density of the frozen polarized material beads.

[b] Helium density.

[c] The first and the second length values correspond to the cell length and the carbon foil thickness, respectively.

[d] Carbon density.

During EG4 the polarized target was placed 1.01 m upstream from the CLAS center to increase the acceptance at low $Q^2$ by reducing the minimum angle for the scattered electrons. The following targets were used: two 1.0-cm long and one 0.5-cm long $NH_3$ target, one 1.0-cm long $ND_3$ target, one 0.216-cm and one 0.108-cm thick $^{12}$C target, and one empty target. The target types during EG4 are defined in Table I. Unless specified otherwise, "empty target" refers to target type 3 [empty cell with helium (1 cm)] hereafter.

An NMR system was used to monitor the polarization of the target during the experiment, but was subject to three systematic uncertainties that limited its suitability for data analysis. First, the NMR coils were wrapped around the outside of the 1.5-cm diameter target cells, while the electron beam was only rastered over the central 1.2-cm portion of the target. The NMR signal was thus dominated by the material at the edges of the cell, and lacked sensitivity to the beam-induced depolarization of the material at the center. This uncertainty is difficult to estimate, as the effect depends on the accumulated dose. Second, for the EG4 experiment the two polarized target cells were adjacent to one another on the insert, as shown in Fig. 4, and cross-talk was observed between the cells' NMR circuits. Tests performed at the end of the experiment indicate that cross-talk could contribute an uncertainty of about 5%–10% to the polarization measurement because of its effect on the thermal-equilibrium calibration of the NMR signal. Third, calibration of the NMR system itself is normally subject to a 4%–5% uncertainty. These three effects added up to a large systematic uncertainty to the target polarization measured by NMR. Therefore, it was decided that the asymmetries of *ep* elastic scattering would be used to extract the product of the beam and target polarizations $P_b P_t$ needed for the exclusive channel analysis reported here. The methods and results for the elastic $P_b P_t$ extraction will be described in Sec. III D. For

$NH_3$, the use of $^{15}N$ has the advantage that only one unpaired proton can be polarized, while all neutrons are paired to spin zero. The polarized proton in the $^{15}N$ does, however, affect the measured asymmetry by a small amount, as discussed in Sec. III G.

## III. DATA ANALYSIS

### A. Exclusive event selection

Exclusive events $\vec{e}\vec{p} \to e'\pi^+(n)$ were identified by detecting the final state electron in coincidence with a pion and using a missing mass cut to select the undetected neutron. For each event, we required that two particles be detected with the correct charges ($-1$ for the electron and $+1$ for the $\pi^+$). Each particle was required to have valid information from DC and TOF, and have reconstructed momentum greater than 0.3 GeV/$c$ (0.1 GeV/$c$ higher than the momentum acceptance of CLAS [36]).

For particle identification, EC and CC signals were used to identify electrons. Cuts were applied on the EC: $E_{\rm tot} > (p - 0.3) \times 0.22, E_{\rm in} > (0.14p - 0.8E_{\rm out})$ and $E_{\rm in} > 0.035p$, where $E_{\rm in}$ and $E_{\rm out}$ are the energy deposited in the inner and the outer layers of the EC, respectively; $E_{\rm tot} = E_{\rm in} + E_{\rm out}$ and $p$ is the particle momentum in GeV/$c$. These cuts were selected to optimize the separation of electrons (that produce electromagnetic showers) from pions (that deposit energy mostly through ionizations). We also required there to be only one hit in the CC, with its signal consistent with those from the EC and the TOF in both hit position and timing.

Pions were determined from a mass cut of $0.01 < m < 0.30$ GeV/$c^2$ and a TOF cut $|t_{\rm TOF} - t^{\pi}_{\rm expected}| < 1.0$ ns. The expected flight time of the pion, $t^{\pi}_{\rm expected}$, was calculated from the particle's momentum in combination with the timing of the electron. Figure 5 shows the effect of the TOF cut on the $\beta \equiv v/c$ vs momentum $p$ distributions, where $v$ is the velocity amplitude (speed) of the particle. The TOF cut used clearly selected pions out of other particle background.

For each event, a vertex $z$ was used. Here $z$ is defined as pointing along the beam direction with the origin coinciding with the CLAS center. The polarized target was positioned upstream of the CLAS center during EG4 (see Fig. 2), and the center of the target was determined from empty target data to be at $z = -101$ cm. The $z$ cut was optimized to be

$$-106 \text{ cm} < z < -96 \text{ cm}, \qquad (22)$$

where the range was determined using empty target data to exclude as much material outside the target as possible. See Fig. 7 in Sec. III C for a detailed presentation of the vertex $z$ distribution.

Acceptance cuts, also called "fiducial cuts," were applied on both electrons and pions using reconstructed DC variables. These acceptance cuts exclude regions where the detector efficiency is not well understood, which often happens on the edge of the detectors, but could also include regions where certain parts of the detectors malfunctioned. Moreover, because the main purpose of EG4 was measurement of the GDH sum, which only requires detection of inclusively scattered electrons, not all six DC sectors were turned on during the run. This caused a variation in the $\phi^*$ acceptance of the exclusive channel. Determination of the acceptance and its effects on the asymmetries will be described in Sec. III H.

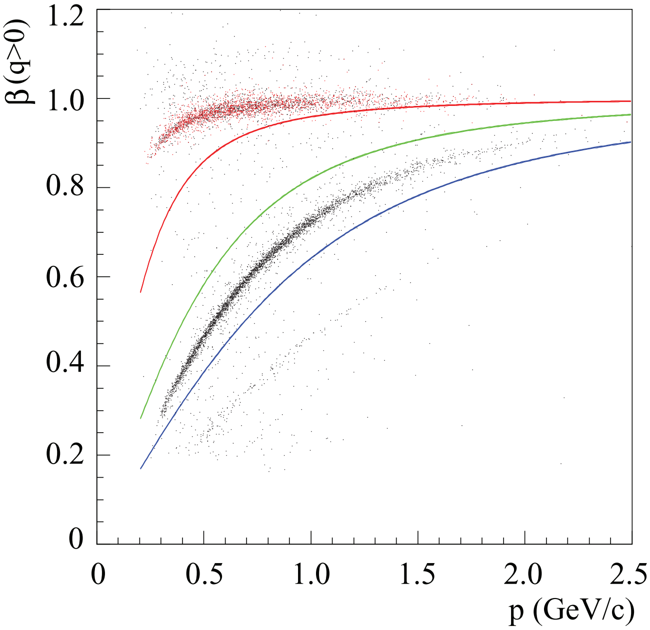

FIG. 5. $\beta$ vs $p$ for all positively charged particles, with (red) and without (black) TOF cut for pions. The red, green, and blue curves correspond to reconstructed masses of 0.3,0.7, and 1.2 GeV/$c^2$, respectively, which are typical cutoff values used to distinguish between pions and kaons, kaons and protons, and protons and heavier particles. As can be seen, the positively charged particles detected consist of significant fractions of protons and heavier particles and a small fraction of kaons, but the ±1.0-ns TOF cut is quite effective in selecting pions. These data were collected on the long top $NH_3$ target during the 3-GeV run period.

### B. Beam properties

As described in the previous section, the helicity of the electron beam followed a quartet structure. For EG4, the beam helicity of each event was delayed by 8 pulses (2 quartets) and then recorded in the data stream. This delayed recording helped to avoid cross-talk between the helicity signal and the electronics or data acquisition system in the hall. In the data analysis, the delay of the helicity sequence was corrected to match each event to its true beam helicity state. During this process, events with inconsistent recording of the helicity sequence were rejected.

A helicity dependence of the integrated beam charge causes a first-order correction to the measured physics asymmetry, and thus it is desired to keep the charge asymmetry as small as possible. The beam charge asymmetry was calculated using the charge measured by the Faraday cup. It was found to be below the percent level throughout the EG4 experiment, and for most runs had stable values at or below the $10^{-3}$ level.

Different methods for deriving the beam energy were used during EG4. The exact energies were 1.054, 1.338, 1.989, 2.260, and 2.999 GeV. The beam polarization was determined

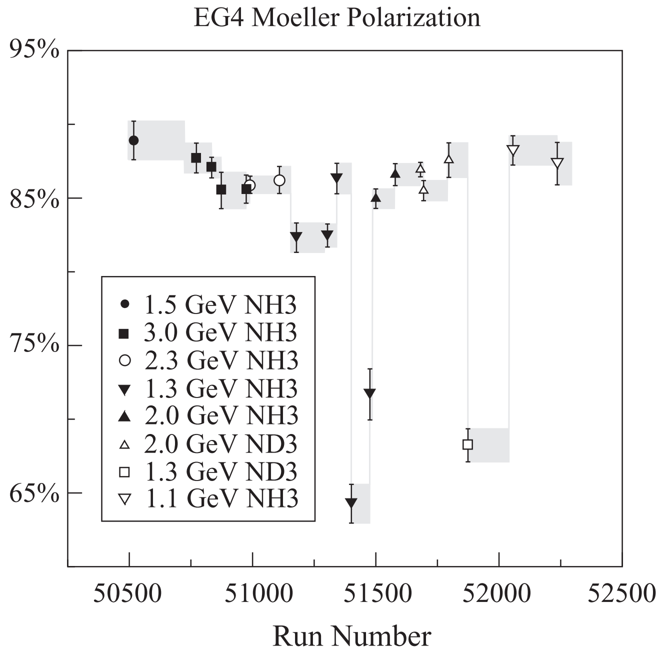

FIG. 6. Beam polarization from Møller measurements vs run number for the whole EG4 experiment. The gray bands represent extrapolations of the beam polarization to the corresponding range of runs as described in the text.

using a Møller polarimeter [36] in Hall B that measured the asymmetry in elastic electron-electron scattering. The results are shown in Fig. 6. Typically, Møller measurements were performed as soon as a change to the beam configuration was made, and then intermittently throughout the run period. Therefore, the beam polarization from each Møller measurement was applied retroactively to runs that immediately follow such configuration changes, and to runs that follow the Møller measurement until the next valid measurement is available. Two additional measurements were done using a Mott polarimeter [41–44], which is located near the injector where the beam electrons have reached 5 MeV in energy but before entering the first linac. The Mott polarimeter results were consistent with those from Møller measurements. The absolute beam helicity was determined using the $\sin\phi^*$-weighted moment of the beam asymmetry $A_{LU}$ in the $\Delta(1232)3/2^+$ region and comparing with results from previous experiments [45,46]. Using the $A_{LU}$ method, it was determined that when the beam IHWP is inserted, for beam energies 1.3 and 2.3 GeV, the positive DAQ helicity corresponds to the true negative helicity of the beam electron, while for other energies the positive DAQ helicity corresponds to the true positive electron helicity. These results are consistent with the sign change of the beam polarization measured with the Møller polarimeter.

### C. Kinematic corrections

Various corrections were applied to the kinematic variables reconstructed from the detectors [47]. The first is the raster correction: To avoid the electron beam overheating the target, the beam was rastered in a circular pattern during EG4 using four magnets located upstream of the target. The values of the magnet current were recorded in the data stream and were used to calculate the beam position $(x,y)$ at the target. The beam position was then used to recalculate the vertex position along the beam direction $z$. After the raster correction was applied, the average value of the $z$ positions of all particles in the same event was taken as the true vertex position of the event; see Fig. 7 [47]. The polar and the azimuthal angles $\theta$ and $\phi$ of each particle were also corrected using the new beam and vertex positions. This procedure took into account the multiple scattering effect that affected the reconstructed vertex position randomly for each particle.

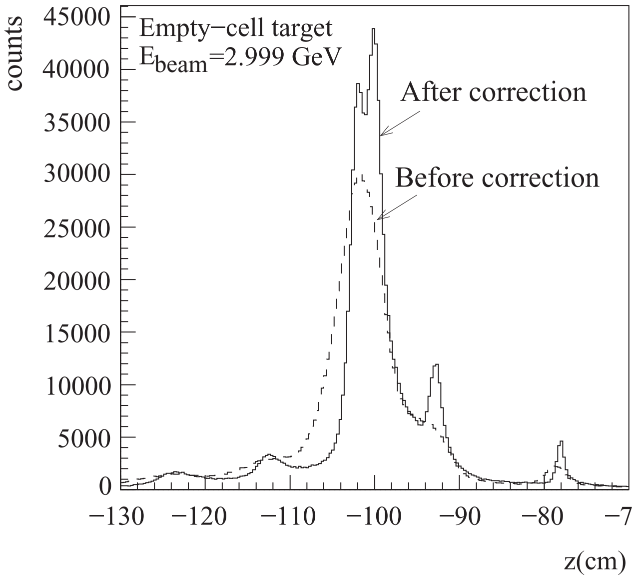

FIG. 7. Electrons' vertex $z$ position before (dashed) and after (solid) raster corrections, taken with the empty target with the 3-GeV beam. While the beam line exit window (at $z = -78.3$ cm) can be seen both before and after the correction, the banjo windows (at $z = -100$ and $-102$ cm), the 4-K heat shield (14 $\mu$m aluminum at $z = -121.0$ cm), some target structure at $z \approx -112$ cm, and several insulating foils (aluminum or aluminized mylar, between $z = -90.5$ and $-94.1$ cm), become visible only after the raster correction. The vertex $z$ cut, Eq. (22), corresponds to slightly more than $3\sigma$ in the target thickness [47].

Because of uncertainties in our knowledge of the drift chamber positions and of the shape and location of the torus coils, a systematic shift of the particle momentum was present. To correct for this shift, the magnitude of the reconstructed particle momentum $p$ and the polar angle $\theta$ were adjusted using sector-dependent parameters. The detailed method for the momentum correction is described in Ref. [48] and results for this experiment are given in Ref. [47]. For sector 6 equipped with the new Cherenkov counter, inclusive elastic $ep$ scattering events were used to optimize the correction based on the invariant mass $W$ position of the elastic peak. For the other sectors, electron triggers were not available and hadrons from exclusive events such as $ep \to e'p'X, ep \to e'\pi^+\pi^-X$, and exclusive events $ep \to e'p'\pi^+\pi^-$ were used to optimize the corrections.

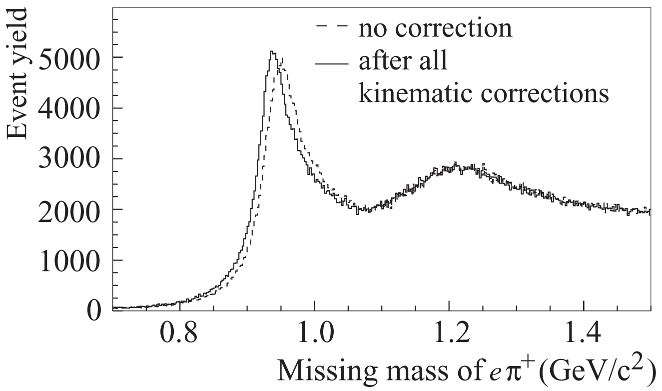

FIG. 8. Missing mass spectrum for the $e + p \to e'\pi^+(X)$ channel before (dashed) and after all kinematics corrections (solid), from six 3.0-GeV long top NH$_3$ target runs. After all corrections, the peak center is closer to the expected value (the neutron mass).

Finally, the momentum of each particle was corrected for the energy loss from passage through material enclosed in the target banjo and the target windows. For electrons a single value $dE/dx = 2.8$ MeV/(g/cm$^2$) was used, while for other particles the Bethe-Bloch equation [49] was used to calculate the ionization loss.

Figure 8 shows the effect on the missing mass spectrum for the $ep \to e'\pi^+(X)$ channel from kinematic corrections.

### D. Elastic scattering for extracting $P_b P_t$

The product of the beam and the target polarizations $P_b P_t$ is needed to directly correct the exclusive channel asymmetries. During EG4, the target polarization $P_t$ was measured by NMR and the beam polarization $P_b$ by the Møller polarimetry. However, because of reasons described in Sec. II C, the NMR measurements had large uncertainties and an alternate method had to be used. For EG4 we extracted $P_b P_t$ for all beam energies by comparing the double-spin asymmetry of elastic $ep$ events to the expected value:

$$P_b P_t = \frac{A^{el}_{\text{meas}}}{A^{el}_{\text{th}}}, \tag{23}$$

where the measured elastic asymmetry was extracted from data using

$$A^{el}_{\text{meas}} = \frac{A^{el}_{\text{raw}}}{f_{el}}, \tag{24}$$

with $f_{el}$ the elastic dilution factor to account for the effect of events scattered from unpolarized material in the target. The raw asymmetry was evaluated as

$$A^{el}_{\text{raw}} = \frac{\frac{N^{el}_R}{Q_R} - \frac{N^{el}_L}{Q_L}}{\frac{N^{el}_R}{Q_R} + \frac{N^{el}_L}{Q_L}}, \tag{25}$$

where $N^{el}_{R(L)}$ and $Q_{R(L)}$ are the elastic event yield and the beam charge for the right- (left-)handed beam electrons, respectively. The expected elastic-scattering asymmetry $A^{el}_{\text{th}}$ was calculated using

$$A^{el}_{\text{th}} = -2\sqrt{\frac{\tau}{1+\tau}}\tan\frac{\theta_e}{2} \times \frac{\left[\sqrt{\tau\left(1+(1+\tau)\tan^2\frac{\theta_e}{2}\right)}\cos\theta_e + \sin\theta_e\frac{G^p_E}{G^p_M}\right]}{\left[\frac{(G^p_E/G^p_M)^2+\tau}{1+\tau} + 2\tau\tan^2\frac{\theta_e}{2}\right]}, \tag{26}$$

with $\tau = Q^2/(4M^2)$. The proton form factor fits from Ref. [50] were used:

$$G^p_E = 1/[1 + 0.62Q + 0.68Q^2 + 2.8Q^3 + 0.83Q^4], \tag{27}$$

and

$$G^p_M = 2.79/[1 + 0.35Q + 2.44Q^2 + 0.5Q^3 + 1.04Q^4 + 0.34Q^5], \tag{28}$$

with $Q \equiv \sqrt{Q^2}$ in GeV/$c$. Using a more updated fit of the proton form factors than Ref. [50] would change the asymmetry value by less than 2% relative.

Elastic events were identified using two methods: (1) inclusive elastic events where only the scattered electron was detected and a cut on the invariant mass $W$ near the proton peak was applied; (2) exclusive elastic events where both the scattered proton and electron were detected and cuts were applied to the electron and the proton azimuthal angles, $|\phi_e - \phi_p - 180^\circ| < 3^\circ$, the polar angles of the proton and the electron's momentum transfer $\vec{q}$, $|\theta_p - \theta_q| < 2^\circ$, and the missing energy $E_{\text{miss}} < 0.15$ GeV. The exclusive analysis had limited statistics and only worked for the 3.0- and the 2.3-GeV data sets. For lower beam energies, the proton's scattering angle was typically greater than 49°, and was blocked by the polarized target coils. Therefore the $P_b P_t$ value extracted from exclusive elastic events was only used as a cross-check of the $P_b P_t$ from inclusive events.

The presence of unpolarized material reduces the measured asymmetry, and this effect is described as a dilution factor in the analysis. The dilution factor for the inclusive elastic events, $f^{\text{incl}}_{el}$, was extracted by comparing the invariant mass $W$ spectrum of the polarized target to that computed for the unpolarized material. The beam-charge-normalized $W$ spectrum for the unpolarized material in the polarized target, denoted as $\frac{N_{\text{NinNH}_3}}{Q_{\text{NH}_3}}$, was calculated using the spectra of the carbon and the empty target, the known thickness and density of the carbon and the empty target, and the polarized target's packing factor $x_{\text{NH}_3}$ defined as the absolute length of the polarized material in the polarized target:

$$\frac{N_{\text{NinNH}_3}}{Q_{\text{NH}_3}} = r_C\frac{N_{^{12}\text{C}}}{Q_{^{12}\text{C}}} + r_{\text{empt}}\frac{N_{\text{empt}}}{Q_{\text{empt}}}, \tag{29}$$

where $N_{^{12}\text{C(empt)}}$ and $Q_{^{12}\text{C(empt)}}$ are the yield and the beam charge of the carbon (empty) target data. The scaling factors are

$$r_C = \frac{\left(B_{\text{NH}_3}\rho_{\text{NH}_3}x_{\text{NH}_3} + B_w\rho_w x_w\frac{x_{\text{NH}_3}}{l}\right)}{B_{^{12}\text{C}}\rho_{^{12}\text{C}}x_{^{12}\text{C}} + B_w\rho_w x_w\frac{x_{^{12}\text{C}}}{l}}, \tag{30}$$

$$r_{\text{empt}} = \left(1 - \frac{x_{\text{NH}_3}}{l}\right) - \left(1 - \frac{x_{^{12}\text{C}}}{l}\right)r_C, \tag{31}$$

TABLE II. Material used for the EG4 target and their locations in increasing order of $z$, in the range $z = (-120, -80)$ cm. The ratios $Z/A$ were used in the dilution factor analysis of the exclusive channel; see Sec. III F.

| Location $z$ (cm) | Material | Density (g/cm$^3$) | Thickness | $Z/A$ |
|---|---|---|---|---|
| $-101.9$ | Banjo entrance window, Al | 2.7 | 71 $\mu$m | 13./26.982 |
| Varies | Target entrance window, kapton | 1.42 | 25 $\mu$m | 0.51264 |
| Varies | $NH_3$ | 0.917 | $x$[a] | 7/18 |
| Varies | Long $^{12}C$ | 2.166 | $2.16 \pm 0.05$ mm | 6/12 |
| Varies | Liquid $^4He$ | 0.145 | $l - x$[a] | 2/4 |
| Varies | Target entrance window kapton | 1.42 | 25 $\mu$m | 0.51264 |
| $-99.6$ | Banjo exit window Al | 2.7 | 71 $\mu$m | 13./26.982 |

[a] $l$ is the banjo length and $x$ is either the packing factor (for $NH_3$ targets) or the carbon foil thickness (for carbon targets).

where $x_{^{12}C}$ is the thickness of the carbon foil in the carbon target, $x_w$ is the sum of thicknesses of other unpolarized material in the target, $l$ is the target banjo length (1.0 cm for the long target and 0.5 cm for the short target), and $B_{^{12}C,w} = 1$ are the bound-nucleon fractions of the carbon target and other unpolarized material in the target, respectively. The values of $x$ for the various materials are given in Table II. The bound-nucleon fraction for the $NH_3$ target takes into account both the fraction of bound nucleons and a correction for the extra neutron in the $^{15}N$: $B_{NH_3} = (14 + \sigma_n/\sigma_N)/18$ with $\sigma_N = (\sigma_p + \sigma_n)/2$ and $\sigma_{p,n}$ are the calculated elastic cross sections for the proton and the neutron, respectively.

After the contribution from the unpolarized material was known, the dilution factor was calculated using

$$f_{el}^{\text{incl}} = \frac{N_{\text{pinNH}_3}}{N_{\text{NH}_3}} = \frac{N_{\text{NH}_3} - N_{\text{NinNH}_3}}{N_{\text{NH}_3}}, \tag{32}$$

where $N_{NH_3}$ is the total number of events from the $NH_3$ target. The dilution correction to the elastic asymmetry was then applied using Eq. (24). In the present analysis, elastic events below $Q^2 = 0.156$ (GeV/$c$)$^2$ could not be used because of electrons scattered elastically from nuclei in the target, such as $^4He$ and nitrogen. These low $Q^2$ bins were rejected in the $P_bP_t$ analysis.

Figure 9 shows the $W$ spectrum decomposition for 1.1- and 3.0-GeV inclusive elastic scattering data for two $Q^2$ bins. The low $Q^2$ bin (top) is to illustrate the effect of the nuclear elastic scattering and these bins were rejected from the $P_bP_t$ analysis. The high $Q^2$ bin (bottom) shows no such effect and the $P_bP_t$ extracted are considered reliable. After the $P_bP_t$ value was extracted for individual $Q^2$ bins, the results were checked to ensure there was no systematic $Q^2$ dependence, which would imply a problem with the analysis. The $P_bP_t$ results were then averaged over all $Q^2$ bins above 0.156 (GeV/$c$)$^2$. This was done for each individual run and the run-by-run, $Q^2$-averaged $P_bP_t$ results were used to correct the asymmetries from the exclusive channel. Figure 10 illustrates the variation of $P_bP_t$ during the experiment.

The uncertainty of the packing factor $x_{NH_3}$ used in the analysis was checked using the $W$ spectrum below $W = 0.9$ (GeV/$c^2$), because an incorrect normalization would yield an over- or an under-subtraction of the yield from unpolarized material. For the 2.3- and 3.0-GeV data the value of $x_{NH_3}$ was confirmed by comparing the $P_bP_t$ value extracted from the inclusive to that from the exclusive elastic events. The packing factor and its uncertainty also affect the dilution analysis of the exclusive channel, to be described in the next sections, thus the final results on $P_bP_t$ for each combination of beam energy and polarized target type are shown together with the exclusive channel dilution results in Table III. The relatively larger error bar for the 1.1-GeV $NH_3$ long bottom target is because most of the data were affected by the nuclear elastic scattering and there are very limited $Q^2$ bins available for the elastic $P_bP_t$ analysis.

In addition to checking the $W$ spectrum and the comparison between inclusive and exclusive elastic events, the $en \to e'\pi^-(p)$ channel was also used to check $x_{NH_3}$ because these events come primarily from the unpolarized neutrons of the nitrogen in the target and thus should have a dilution factor of zero. The $e'\pi^-(p)$ events were analyzed for all beam energies and it was found the dilution factors calculated using the $x_{NH_3}$ values in Table III were indeed consistent with zero. As a last check, the run-by-run values of $P_bP_t$ were compared with the numerous target material and configuration changes during the experiment, and were found to be consistent with the physical changes of the target.

### E. Extraction of exclusive channel asymmetries

To extract the exclusive channel asymmetries, the $e'\pi^+(n)$ channel events were divided into four-dimensional bins in $W, Q^2, \cos\theta^*$, and $\phi^*$ and then the asymmetries were extracted from the counts in each bin. The event counts for the four combinations of beam helicities and target polarization can be written, based on Eq. (5), as

$$N_{\uparrow\Uparrow} = D_1\big[\sigma_0 + P_b^{\Uparrow}\sigma_e + f_{\text{dil}}^{\pi}P_t^{\Uparrow}\sigma_t + P_b^{\Uparrow}f_{\text{dil}}^{\pi}P_t^{\Uparrow}\sigma_{et}\big], \tag{33}$$

$$N_{\downarrow\Uparrow} = D_2\big[\sigma_0 - P_b^{\Uparrow}\sigma_e + f_{\text{dil}}^{\pi}P_t^{\Uparrow}\sigma_t - P_b^{\Uparrow}f_{\text{dil}}^{\pi}P_t^{\Uparrow}\sigma_{et}\big], \tag{34}$$

$$N_{\uparrow\Downarrow} = D_3\big[\sigma_0 + P_b^{\Downarrow}\sigma_e - f_{\text{dil}}^{\pi}P_t^{\Downarrow}\sigma_t - P_b^{\Downarrow}f_{\text{dil}}^{\pi}P_t^{\Downarrow}\sigma_{et}\big], \tag{35}$$

$$N_{\downarrow\Downarrow} = D_4\big[\sigma_0 - P_b^{\Downarrow}\sigma_e - f_{\text{dil}}^{\pi}P_t^{\Downarrow}\sigma_t + P_b^{\Downarrow}f_{\text{dil}}^{\pi}P_t^{\Downarrow}\sigma_{et}\big], \tag{36}$$

where the arrows in the subscripts of $N$ are for the beam helicities ($\uparrow$ or $\downarrow$) and the target spin directions ($\Uparrow$ or $\Downarrow$), respectively, with $\uparrow$ and $\Uparrow$ being positive helicity or parallel to the beam direction and $\downarrow$ and $\Downarrow$ being negative helicity or antiparallel to the beam direction. The parameters $P^{\Uparrow}$ and $P^{\Downarrow}$ are the statistically averaged target or beam polarizations when the target spin is aligned and antialigned to the beamline, respectively. The dilution factor $f_{\text{dil}}^{\pi}$ for the exclusive channel

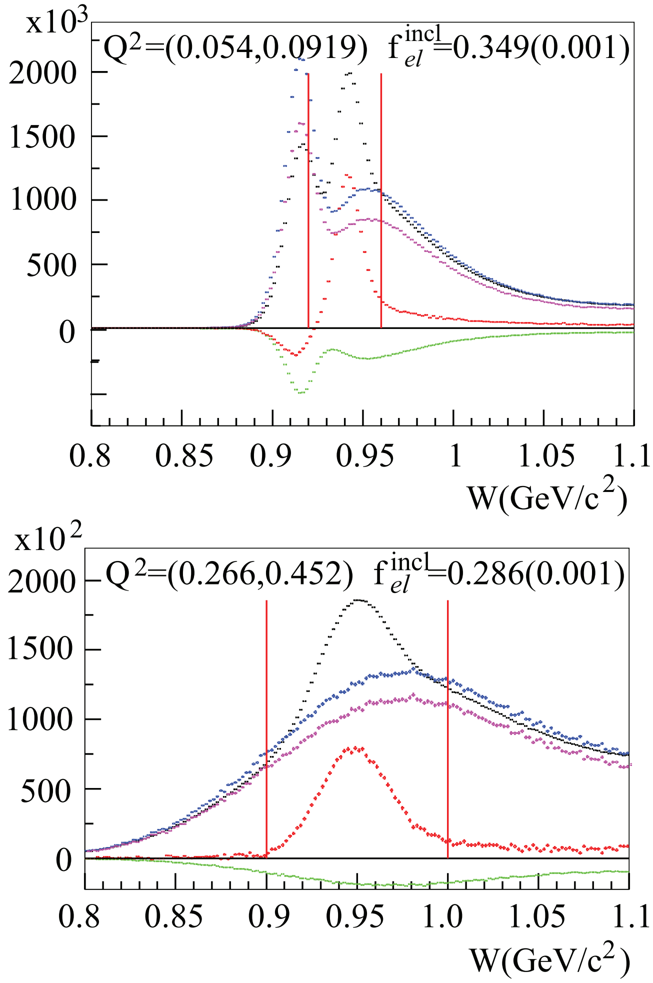

FIG. 9. $W$ spectrum for dilution calculation for inclusive elastic $P_bP_t$ analysis. (Top) 1.1-GeV data on $NH_3$ long bottom target in the $Q^2 = (0.054,0.092)$ $(\mathrm{GeV}/c)^2$ bin; (bottom) 3.0-GeV data on $NH_3$ long top target in the $Q^2 = (0.266,0.452)$ $(\mathrm{GeV}/c)^2$ bin. For each panel, histograms from the carbon target (blue) and empty target (green) were scaled using Eqs. (30) and (31) using a packing factor of 0.75 cm for 1.1 GeV and 0.65 cm for 3.0 GeV, respectively, and their sum gave the estimated contribution from unpolarized material in the $NH_3$ target (magenta). This unpolarized background was then subtracted from the $NH_3$ spectrum (black) to estimate the contribution from polarized protons in the target (red). The calculated elastic dilution factors are shown for each set of data with their uncertainties in the brackets. The $W$ cuts used to select elastic events are shown as the two red vertical lines. Note that the scaled empty target spectrum (green) is negative, indicating that for the chosen packing factor we have scaled up the carbon data and then subtracted the extra helium to reproduce the unpolarized background in $NH_3$. For $Q^2$ bins below 0.156 $(\mathrm{GeV}/c)^2$, the nuclear elastic event contaminates the $ep$ elastic peak and the extraction of the dilution factor is not reliable. For this reason, data with $Q^2 < 0.156\,(\mathrm{GeV}/c)^2$ were rejected from the elastic $P_bP_t$ analysis.

$\vec{e}\vec{p} \to e'\pi^+(n)$ is defined as the fractional yield from the polarized proton in the $NH_3$ target, which effectively changes the target polarization. The four parameters $D_{1,2,3,4}$, relating event counts to cross sections, are related to the total beam charge, target thickness, spectrometer acceptance, and detector efficiencies for each configuration. For stable running periods with no significant change in the target cell, the spectrometer setting and the detector status, the $D$ factor is strictly proportional to the accumulated beam charge in each setting. From Eqs. (33)–(36), one can form the asymmetries as

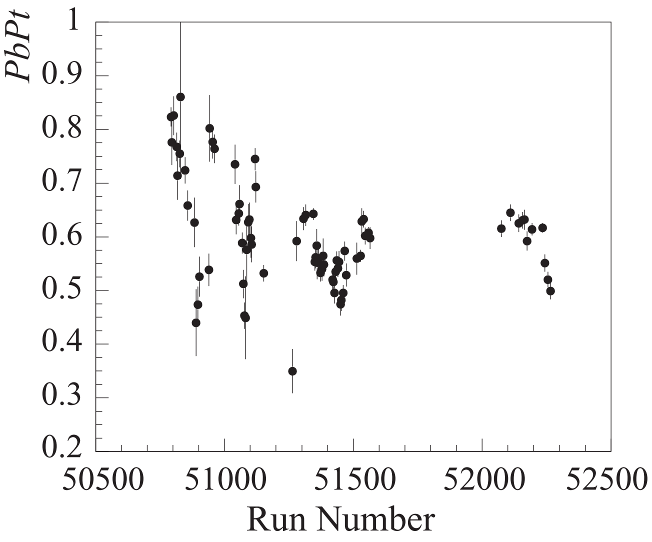

FIG. 10. Magnitude of $P_bP_t$ extracted from inclusive elastic scattering events for all runs used in the present analysis that were taken on the polarized $NH_3$ target. For illustration purposes, results from adjacent runs that shared the same beam insertable half-wave plate status were combined and are shown as one data point here. The error bars shown are statistical uncertainties determined by the number of available elastic events.

$$A_{LU} = \frac{1}{P_b^{\Uparrow}P_b^{\Downarrow}} \times \left[\frac{\left(\frac{N_{\uparrow\Downarrow}}{D_3} - \frac{N_{\downarrow\Downarrow}}{D_4}\right)P_b^{\Uparrow}P_t^{\Uparrow} + \left(\frac{N_{\uparrow\Uparrow}}{D_1} - \frac{N_{\downarrow\Uparrow}}{D_2}\right)P_b^{\Downarrow}P_t^{\Downarrow}}{\left(\frac{N_{\uparrow\Uparrow}}{D_1} + \frac{N_{\downarrow\Uparrow}}{D_2}\right)P_t^{\Downarrow} + \left(\frac{N_{\uparrow\Downarrow}}{D_3} + \frac{N_{\downarrow\Downarrow}}{D_4}\right)P_t^{\Uparrow}}\right], \tag{37}$$

$$A_{UL} = \frac{1}{f_{\mathrm{dil}}^{\pi}} \frac{\left(\frac{N_{\uparrow\Uparrow}}{D_1} + \frac{N_{\downarrow\Uparrow}}{D_2}\right) - \left(\frac{N_{\uparrow\Downarrow}}{D_3} + \frac{N_{\downarrow\Downarrow}}{D_4}\right)}{\left(\frac{N_{\uparrow\Uparrow}}{D_1} + \frac{N_{\downarrow\Uparrow}}{D_2}\right)P_t^{\Downarrow} + \left(\frac{N_{\uparrow\Downarrow}}{D_3} + \frac{N_{\downarrow\Downarrow}}{D_4}\right)P_t^{\Uparrow}}, \tag{38}$$

$$A_{LL} = \frac{1}{P_b^{\Uparrow}P_b^{\Downarrow}f_{\mathrm{dil}}^{\pi}} \times \left[\frac{\left(\frac{N_{\uparrow\Downarrow}}{D_3} - \frac{N_{\downarrow\Downarrow}}{D_4}\right)P_b^{\Uparrow} - \left(\frac{N_{\uparrow\Uparrow}}{D_1} - \frac{N_{\downarrow\Uparrow}}{D_2}\right)P_b^{\Downarrow}}{\left(\frac{N_{\uparrow\Uparrow}}{D_1} + \frac{N_{\downarrow\Uparrow}}{D_2}\right)P_t^{\Downarrow} + \left(\frac{N_{\uparrow\Downarrow}}{D_3} + \frac{N_{\downarrow\Downarrow}}{D_4}\right)P_t^{\Uparrow}}\right]. \tag{39}$$

### F. Dilution factor for the exclusive channel

In contrast to the dilution for inclusive $P_bP_t$ analysis that has only $Q^2$ dependence (Sec. III D), the dilution for exclusive pion production could vary with all four kinematic variables $W, Q^2, \cos\theta^*$, and $\phi^*$ [51]. To evaluate the dilution factor for all four-dimensional bins of $(W, Q^2, \cos\theta^*, \phi^*)$, the yield from the unpolarized material inside the polarized $NH_3$ target was

TABLE III. Dilution factor $f_{\rm dil}^{\pi^+}$ and the product $P_bP_tf_{\rm dil}^{\pi^+}$ for the exclusive $\pi^+$ channel. The $P_bP_t$ results extracted from inclusive elastic scattering, described in Sec. III D, and their uncertainties are also shown. For $P_bP_t$, the three errors are from statistical uncertainty of the elastic events, the statistical uncertainty of the carbon and empty target counts used to calculate the dilution factor for inclusive elastic analysis, and the uncertainty of the packing factor. $P_bP_t$ values from Møller and NMR measurements are shown for comparison, although the NMR measurements are unreliable as described in Sec. II C. The products $P_bP_tf_{\rm dil}$ are used to correct the exclusive channel asymmetries. The total uncertainties in $P_bP_tf_{\rm dil}$ include uncertainties of $P_bP_t$, statistical uncertainties of $f_{\rm dil}^{\pi^+}$, and the uncertainties from the packing factor (p.f.), all added in quadrature. These total uncertainties will be used as systematic uncertainties on the extracted exclusive channel asymmetries.

| $E_{\rm beam}$ (GeV) | Target ($NH_3$) | p.f. (cm) | $(P_bP_t)_{el}$ | Møller× NMR | $f_{\rm dil}^{\pi^+}$ ±(stat.)±(p.f.) | $P_bP_tf_{\rm dil}$ | $\frac{\Delta(P_bP_tf_{\rm dil})}{P_bP_tf_{\rm dil}}$ (total) |
|---|---|---|---|---|---|---|---|
| 3.0 | Top | $0.65 \pm 0.05$ | $0.614 \pm 0.006 \pm 0.015 \pm 0.045$ | 0.620 | $0.424 \pm 0.021 \pm 0.013$ | 0.260 | 7.0% |
| 2.3 | Top | $0.65 \pm 0.05$ | $0.597 \pm 0.006 \pm 0.021 \pm 0.028$ | 0.551 | $0.476 \pm 0.021 \pm 0.011$ | 0.284 | 6.2% |
| | Short | $0.30 \pm 0.05$ | $0.560 \pm 0.009 \pm 0.026 \pm 0.067$ | 0.601 | $0.322 \pm 0.017 \pm 0.021$ | 0.180 | 9.0% |
| 2.0 | Top | $0.65 \pm 0.05$ | $0.605 \pm 0.004 \pm 0.016 \pm 0.030$ | 0.545 | $0.495 \pm 0.020 \pm 0.010$ | 0.299 | 5.7% |
| | Bottom | $0.65 \pm 0.05$ | $0.636 \pm 0.019 \pm 0.016 \pm 0.031$ | 0.560 | $0.484 \pm 0.021 \pm 0.010$ | 0.308 | 6.4% |
| 1.3 | Top | $0.70 \pm 0.05$ | $0.571 \pm 0.003 \pm 0.009 \pm 0.033$ | 0.509 | $0.494 \pm 0.019 \pm 0.010$ | 0.282 | 5.7% |
| | Bottom | $0.70 \pm 0.05$ | $0.535 \pm 0.003 \pm 0.010 \pm 0.028$ | 0.458 | $0.493 \pm 0.019 \pm 0.010$ | 0.264 | 5.5% |
| | Short | $0.30 \pm 0.05$ | $0.552 \pm 0.010 \pm 0.030 \pm 0.060$ | 0.581 | $0.383 \pm 0.016 \pm 0.014$ | 0.211 | 10.2% |
| 1.1 | Bottom | $0.75 \pm 0.10$ | $0.568 \pm 0.002 \pm 0.007 \pm 0.080$ | 0.563 | $0.496 \pm 0.020 \pm 0.020$ | 0.282 | 11.1% |

constructed using the missing mass spectra from the carbon and the empty targets. Scaling factors for the carbon and empty target data were calculated following a prescription similar to Eqs. (29)–(31), but with the bound-nucleon fraction $B$ replaced by the ratio $Z/A$ (Table II) for the $ep \to e'\pi^+(n)$ $[(1-Z/A)$ for the $en \to e'\pi^-(p)]$ channel. For $NH_3$ one should use $\frac{Z_{\rm NH_3}}{A_{\rm NH_3}} = 7/18$ to account for only unpolarized protons. We obtain

$$\frac{N_{\rm NinNH_3}}{Q_{\rm NH3}} = a\left(\frac{N_{^{12}\rm C}}{Q_{^{12}\rm C}}\right) + b\left(\frac{N_{\rm empt}}{Q_{\rm empt}}\right), \tag{40}$$

where

$$a = \frac{\left(\frac{Z_{\rm NH_3}}{A_{\rm NH_3}}\rho_{\rm NH_3}x_{\rm NH_3}\right) + \left(\frac{Z_w}{A_w}\rho_w x_w\right)\frac{x_{\rm NH_3}}{l}}{\left(\frac{Z_{^{12}\rm C}}{A_{^{12}\rm C}}\rho_{^{12}\rm C}x_{^{12}\rm C}\right) + \left(\frac{Z_w}{A_w}\rho_w x_w\right)\frac{x_{^{12}\rm C}}{l}}, \tag{41}$$

$$b = \left(1 - \frac{x_{\rm NH_3}}{l}\right) - \left(1 - \frac{x_{^{12}\rm C}}{l}\right)a. \tag{42}$$

Similar to elastic analysis, the value of $b$ from Eq. (42) could be either positive or negative depending on the input packing factor. Figure 11 shows the dilution factor evaluation for the 3.0-GeV data using the $NH_3$ long top target.

From Eqs. (38) and (39) one can see that the uncertainties in $P_bP_t$ and $f_{\rm dil}^{\pi}$ should be evaluated at the same time because both depend on the packing factor. Table III shows all $P_bP_t$ and dilution results for the packing factor range used in the elastic $P_bP_t$ analysis. For each setting of beam energy and target, we varied the packing factor by one standard deviation and evaluated $P_bP_t$ and $f_{\rm dil}^{\pi^+}$. We used the observed difference in the product $P_bP_tf_{\rm dil}^{\pi^+}$ as the uncertainty from the packing factor, labeled as $P_bP_tf_{\rm dil}^{\pi^+} \pm (p.f.)$. For the total uncertainty $\frac{\Delta(P_bP_tf_{\rm dil})}{P_bP_tf_{\rm dil}}$ (total), we added the following terms in quadrature: (1) statistical uncertainty of inclusive elastic events used in the $P_bP_t$ analysis; (2) statistical uncertainty of the carbon and empty target counts used to calculate the dilution factor for inclusive elastic events; (3) statistical uncertainty in the exclusive $ep \to e'\pi^+(n)$ channel from limited statistics of carbon and empty target data $f_{\rm dil}^{\pi^+}$ ±(stat.); and (4) the observed variation in $P_bP_tf_{\rm dil}^{\pi^+}$ when the input packing factor was varied within its uncertainty. The resulting total uncertainties on $P_bP_tf_{\rm dil}^{\pi^+}$ were used for the evaluation of the uncertainty of the double-spin asymmetry $A_{LL}$. For the target asymmetry $A_{UL}$, the uncertainty was evaluated by combining the uncertainty of $P_bP_tf_{\rm dil}^{\pi^+}$ and the uncertainty of the Møller measurements on the beam polarization. The uncertainty from the polarizations and the dilution is the largest systematic uncertainty of the present analysis.

The uncertainty in the input packing factor of Table III was checked using not only the $W$ spectrum of elastic events (as described in Sec. III D), but also the dilution factor of the $en \to e'\pi^-(p)$ channel analyzed using a similar prescription as Eqs. (40)–(42). The dilution factor of the $\pi^-(p)$ channel should be consistent with zero in all kinematic bins. Overall, the lower bound in the packing factor was cross-checked between the $en \to e'\pi^-(p)$ dilution result and the elastic $W$ spectrum, and the upper bound in the packing factor was determined always by the elastic $W$ spectrum.

The kinematics dependence of the dilution factor on $Q^2, W$, and the pion center-of-mass angles $\theta^*$ and $\phi^*$ have been studied, and multidimensional fits of the dependence were performed. The limited statistics of the carbon and the empty target data prevented fitting the $(Q^2, W, \cos\theta^*, \phi^*)$ dependence simultaneously. Instead, two bi-dimensional fits were used, one for the $(Q^2, W)$ dependence and one for the $(\cos\theta^*, \phi^*)$ dependence, with the following *ad hoc* parametrizations:

$$\begin{aligned} f_1 = {} & p_0[1 + p_1(Q^2) + p_2(Q^2)^2] \\ & \times [1 + p_3(W - 1.8) + p_4(W - 1.8)^2] \\ & \times \left[1 + \frac{p_5}{(W^2 - 1.50^2)^2 + 1.50^2 \times 0.05^2}\right] \\ & \times \left[1 + \frac{p_6}{(W^2 - 1.68^2)^2 + 1.68^2 \times 0.05^2}\right], \end{aligned} \tag{43}$$

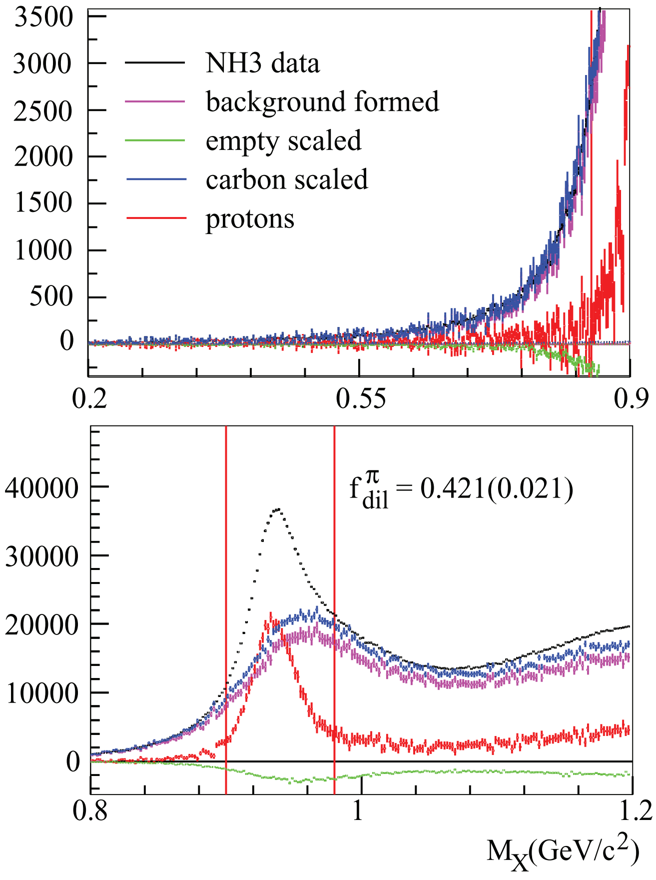

FIG. 11. Missing mass $M_X$ spectrum for deriving the dilution factor for the $ep \to e'\pi^+(n)$ channel. (Top) Missing mass below the neutron mass peak; (bottom) missing mass around the neutron mass peak. The data shown are for the 3.0-GeV run period using the NH$_3$ long top target. Here, the $M_X$ spectrum for the nuclear material (magenta) in the polarized NH$_3$ target was constructed using the spectra for the carbon target (blue), the empty target (green), with an input packing factor $x = 0.65$ cm. The nuclear contribution was then subtracted from the NH$_3$ target spectrum (black) to give the polarized-proton spectrum (red). The dilution factor was evaluated using the region around the neutron peak and is shown in the bottom panel with the uncertainty in the bracket. The histogram and the dilution uncertainties include both statistical uncertainties and the uncertainty in the scaling or packing factors. Note that the empty target (green) spectrum is negative, indicating we have scaled up the carbon data and then subtracted the extra helium (empty target) to reproduce the unpolarized background in NH$_3$. Results for the dilution factor is shown in the bottom plot. The $M_X$ cuts (0.90,0.98) GeV/$c^2$ used in the dilution and the asymmetry analysis are shown by the two red vertical lines.

where $W$ is in GeV/$c^2$ and

$$f_2 = p_0' \times \left[1 + \frac{p_7}{1 - \cos\theta^*}\right][1 + p_8 \sin\phi^* + p_9 \cos\phi^*]. \tag{44}$$

The resulting two fits were then multiplied to give the overall $2 \times 2$-dimensional fit for $f^{\pi}_{\rm dil}(W, Q^2, \cos\theta^*, \phi^*)$. To check the validity of the fit, the results from $f^{\pi}_{\rm dil}(W, Q^2, \cos\theta^*, \phi^*)$ were integrated over three of the four variables, and then compared with the dilution extracted directly from data binned in the fourth variable. This comparison is shown in Fig. 12. One can see that the dilution factors obtained from this method agree with data very well. The $2 \times 2$-dimensional fit $f^{\pi}_{\rm dil}(W, Q^2, \cos\theta^*, \phi^*)$ was used to correct the asymmetries $A_{UL}$ and $A_{LL}$ for the specific $W, Q^2, \cos\theta^*, \phi^*$ bin using Eqs. (38) and (39).

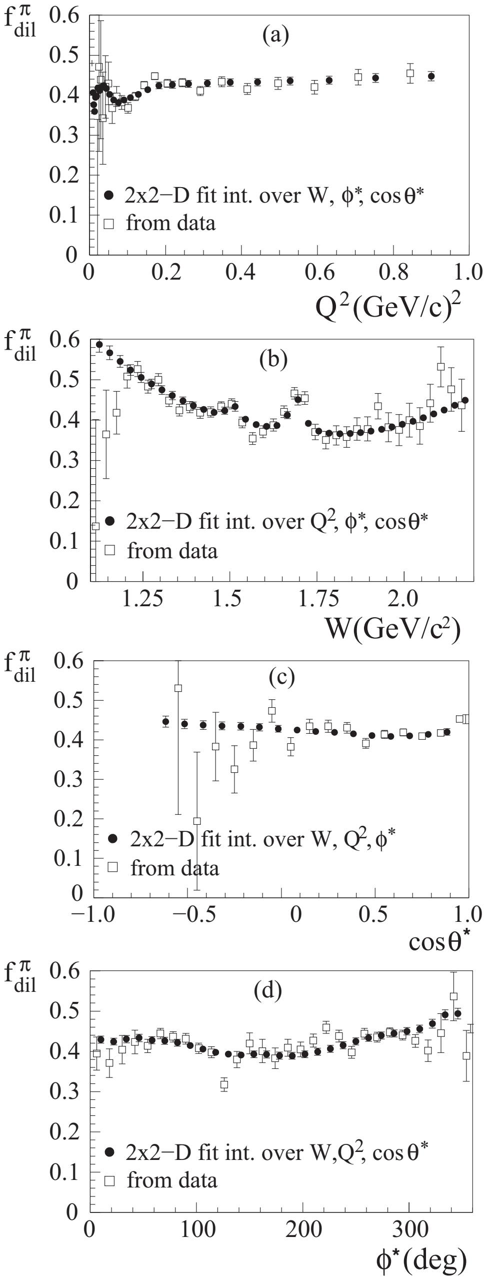

FIG. 12. Dependence of dilution on (a) $Q^2$, (b) $W$, (c) $\cos\theta^*$, and (d) $\phi^*$, for the 3.0-GeV NH$_3$ long top target, $ep \to e'\pi^+(n)$ channel, obtained directly from the data (open squares) and from multiplying the two 2D fits of Eqs. (43) and (44) then integrating over three of the four variables (solid circles). The error bars for the dilution extracted from data are statistical only.

### G. Effect of nitrogen polarization on the asymmetry

The $^{15}$N in the NH$_3$ target is polarizable and can affect the measured asymmetry. In this section we estimate this effect and show that it is negligible. Therefore no correction was made to the extracted exclusive channel asymmetries.

The nitrogen polarization in $^{15}$NH$_3$ can be estimated based on the equal spin temperature (EST) prediction [39]:

$$P(^{15}\mathrm{N}) = \tanh\frac{\mu_{^{15}\mathrm{N}}B}{kT_S}, \quad P(\mathrm{H}) = \tanh\frac{\mu_p B}{kT_S}, \qquad (45)$$

where $\mu_{^{15}\mathrm{N}}$ and $\mu_p$ are the magnetic moments of the $^{15}$N and the proton, respectively, $B$ is the magnetic field of the target, $k$ is the Boltzmann constant, and $T_S$ is the spin temperature that describes the Boltzmann distribution of spins inside the target. The EST prediction was demonstrated to apply to the $^{15}$N and H of the ammonia molecule by several experiments starting with the Spin Muon Collaboration [52]. The SLAC E143 collaboration performed an empirical fit and showed [53]

$$P_{^{15}\mathrm{N}} = 0.136|P_p| - 0.183|P_p|^2 + 0.335|P_p|^3, \qquad (46)$$

which gives $P_{^{15}\mathrm{N}} \approx -15\%$ when $P_p = 90\%$ and $P_{^{15}\mathrm{N}} \approx -8.8\%$ when $P_p = 70\%$. The $^{15}$N polarization is carried by the unpaired proton and its effect relative to the three free protons in NH$_3$ is

$$\Delta P = \frac{1}{3}\left(-\frac{1}{3}\right)P(^{15}\mathrm{N}), \qquad (47)$$

where the additional factor of $-1/3$ comes from the wave function of the unpaired proton in the $^{15}$N [54]. The effect on the asymmetry from the polarized proton in the $^{15}$N is thus at the 1%–2% level, and is negligible compared to the statistical uncertainty of the asymmetry and the systematic uncertainty from the polarizations and the dilution factor.

### H. Acceptance corrections

When studying how the asymmetries vary with very small bins in all four kinematic variables—the electron's $Q^2, W$ and the pion's center-of-mass angles $\theta^*$ and $\phi^*$—the effect of the detector acceptance and efficiency in principle cancel and therefore do not affect the interpretation of the asymmetry results. The effect of acceptance only becomes relevant when integration of the asymmetry over a subset of these four variables is necessary, which is the case for all results presented in Sec. IV.

For results presented in Sec. IV, we evaluated the acceptance of each bin based on acceptance cuts for both electrons and pions. The acceptance correction was then applied on an event-by-event basis: Instead of using the measured counts $N_{\uparrow\Uparrow,\uparrow\Downarrow,\downarrow\Uparrow,\downarrow\Downarrow}$, where each event counts as 1, we first divided 1 by the acceptance of that particular event, then the sum was taken and used as $N_{\uparrow\Uparrow,\uparrow\Downarrow,\downarrow\Uparrow,\downarrow\Downarrow}$ in the formula from Sec. III E, Eqs. (37)–(39). The asymmetries extracted this way were integrated over certain kinematic ranges and compared directly with theoretical predictions. Zero-acceptance bins could not be corrected this way when integrating the data. When integrating the theoretical calculations, we excluded bins where there were no data, and thus removed the zero-acceptance bins from the theory curves as well.

TABLE IV. Summary of systematic uncertainties from the target and beam polarizations and the dilution factor for different beam and target combinations. The 1%–2% relative uncertainty from $^{15}$N and the ±0.03 absolute uncertainty from radiative corrections must be added in quadrature to the values here to obtain the total systematic uncertainty.

| $E_{\mathrm{beam}}$ (GeV) | Target (NH$_3$) | $\Delta A_{UL}/A_{UL}$ (syst) | $\Delta A_{LL}/A_{LL}$ (syst) |
|---|---|---|---|
| 3.0 | Top | 7.0% | 7.0% |
| 2.3 | Top | 6.2% | 6.3% |
| | Short | 9.0% | 9.0% |
| 2.0 | Top | 5.7% | 5.8% |
| 1.3 | Top | 5.7% | 5.9% |
| | Bottom | 5.5% | 5.7% |
| 1.1 | Bottom | 11.1% | 11.2% |

### I. Radiative corrections

Radiative corrections were calculated for both $A_{UL}$ and $A_{LL}$ using the code EXCLURAD [55] and the MAID2007 model [13]. It was found that overall the correction is fairly small and typically no larger than 0.03. Considering the size of the statistical uncertainty of the measurement, radiative corrections were not applied to the asymmetries, but rather are quoted as a systematic uncertainty of $\Delta A = \pm 0.03$ throughout the accessed kinematics.

### J. Summary of all systematic uncertainties

The systematic uncertainty of the $\vec{e}\vec{p} \to e'\pi^+(n)$ exclusive channel is dominated by that from the product $P_b P_t f_{\mathrm{dil}}^{\pi^+}$, shown in Table III. The uncertainty of $P_b P_t f_{\mathrm{dil}}^{\pi^+}$ takes into account the uncertainties in the target packing factor, as well as the thickness and density of various materials in the target. Other non-neglible systematic uncertainties include a relative ±1%–2% from the $^{15}$N in NH$_3$ and a ±0.03 from radiative corrections. Adding these uncertainties in quadrature, we arrive at Table IV for our asymmetry results. For the asymmetry $A_{UL}$, one does not need to normalize by $P_b$. We relied on the elastic $P_b P_t$ results and combined in quadrature their uncertainties with the uncertainty in the Møller polarization to obtain the uncertainty on $P_t$ alone.

## IV. ASYMMETRY RESULTS

Results for the target asymmetry $A_{UL}$ and the double-spin asymmetry $A_{LL}$ are available on a four-dimensional grid of $Q^2, W, \cos\theta^*$, and $\phi^*$. There are 42 $Q^2$ bins logarithmically spaced between 0.00453 and 6.45 (GeV/$c$)$^2$,38 $W$ bins between 1.1 and 2.21 GeV/$c^2$,30 $\phi^*$ bins between 0 and 360°, and 20 $\cos\theta^*$ bins between $-1$ and 1. This binning scheme is referred to as "asymmetry bins." To allow a meaningful comparison with theoretical calculations, we integrated the data over 3 $Q^2$ bins, 8 $W$ bins, 5 $\phi^*$ bins, and 5 $\cos\theta^*$ bins. These will be referred to as "combined bins" hereafter. The resulting combined $W$ bins are (1.1,1.34),(1.34,1.58), and (1.58,1.82) GeV/$c^2$, allowing an examination of the first, the second, and the third nucleon resonance regions, respectively.

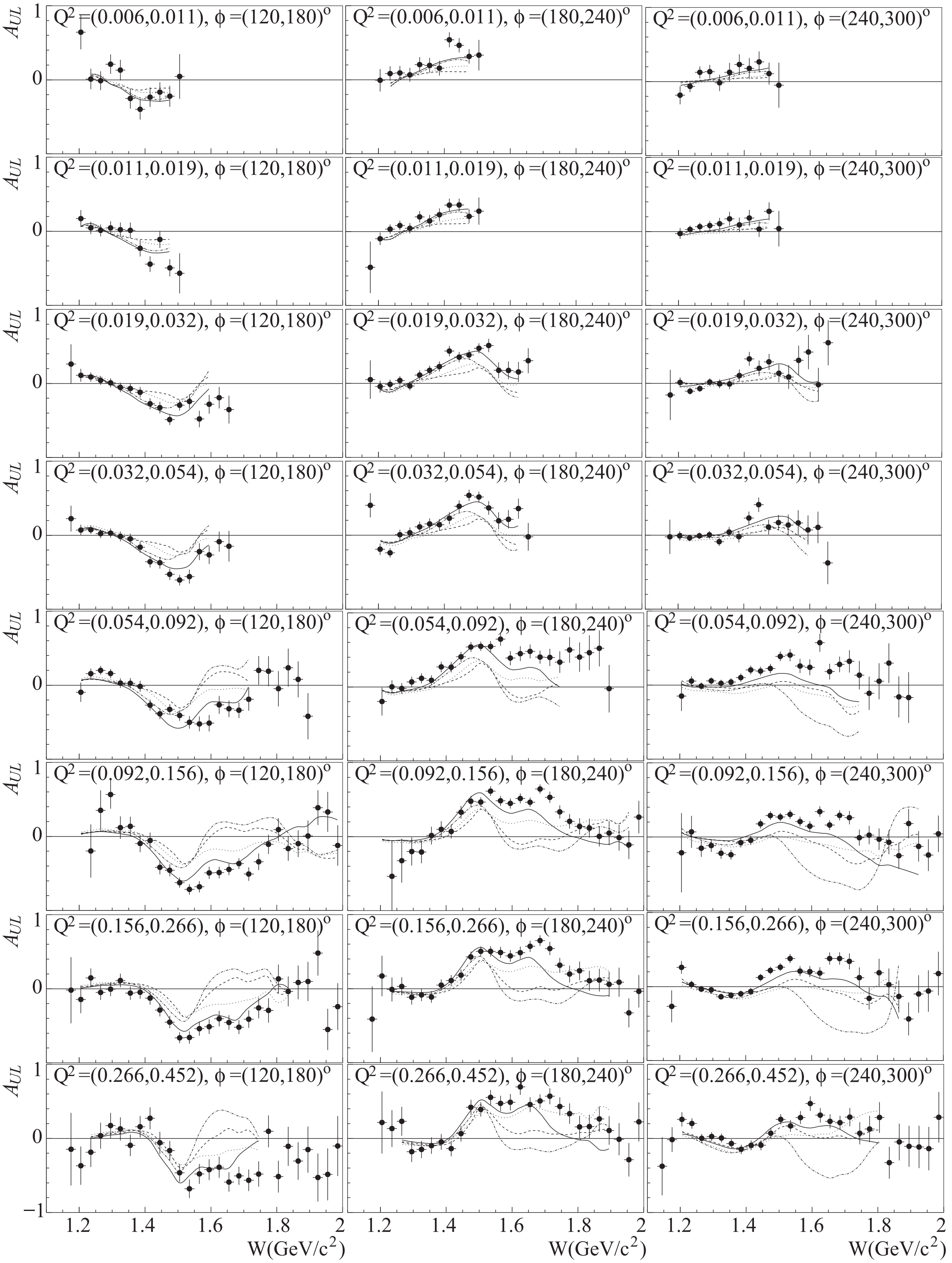

FIG. 13. Results on the target spin symmetries $A_{UL}$ for the $\vec{e}\vec{p} \to e\pi^+(n)$ channel as a function of the invariant mass $W$ in GeV/$c^2$, integrated over $\cos\theta^* = (0.5,1.0)$, in increasing $Q^2$ ranges and three 60° $\phi^*$ bins. From top to bottom the $Q^2$ bins are (0.00646,0.0110) and (0.0110,0.0187) (1.1 GeV $NH_3$ long bottom target), (0.0187,0.0317) and (0.0317,0.054) (1.3 GeV $NH_3$ long top target), (0.054,0.0919) (2.0 GeV $NH_3$ long top target), (0.0919,0.156),(0.156,0.266), and (0.266,0.452) (GeV/$c$)$^2$ (3.0 GeV $NH_3$ long top target). From left to right the $\phi^*$ bins are $\phi^* = (120^\circ,180^\circ),(180^\circ,240^\circ)$, and $(240^\circ,300^\circ)$. In each panel, the horizontal scale is from 1.1 to 2 GeV/$c^2$ in $W$ and the vertical scale is from −1 to 1. Data are compared to four calculations: MAID2007 (solid) [13], JANR (dashed) [14], SAID (dash-dotted) [15], and DMT2001 (dotted) [16].

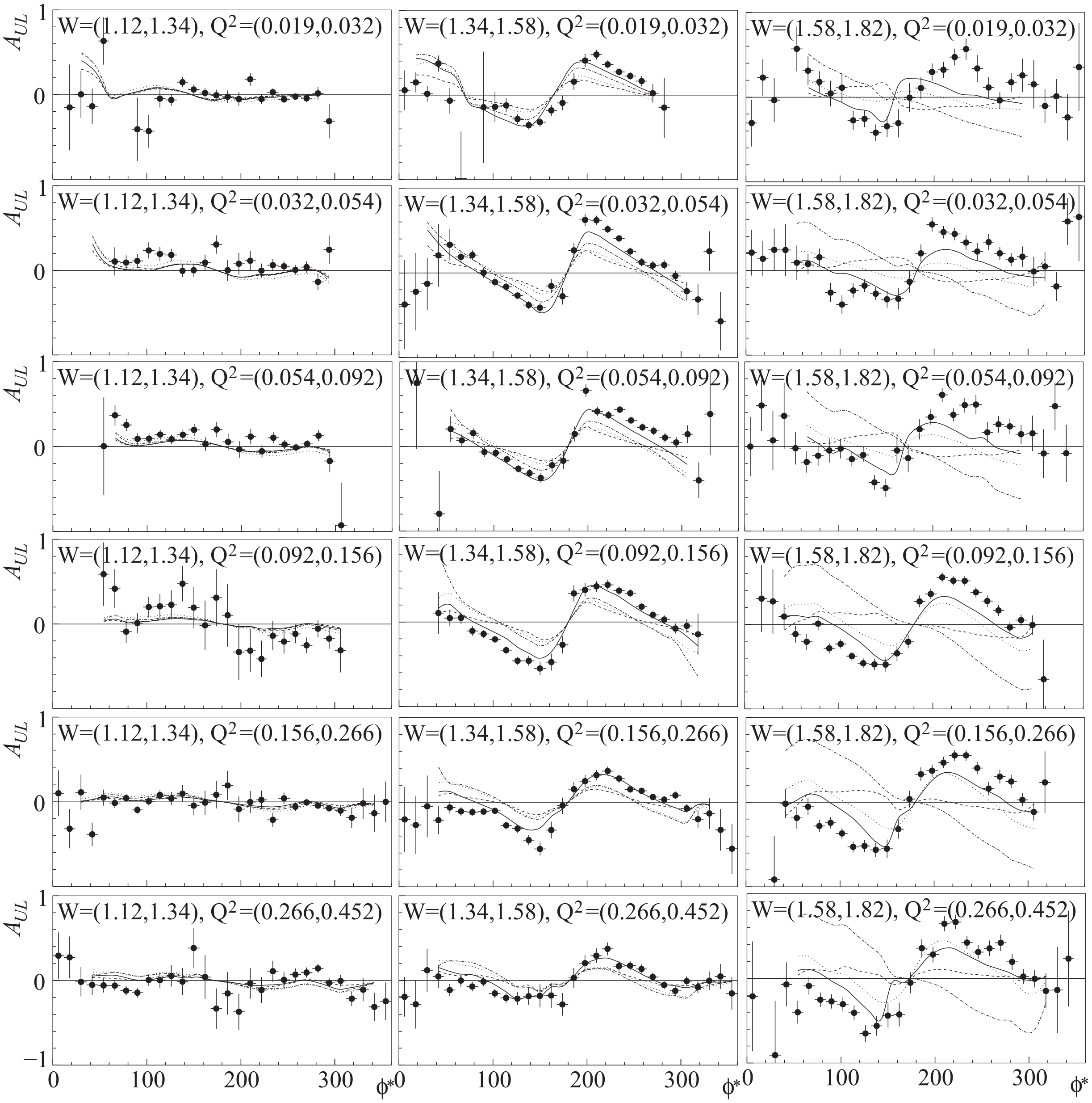

FIG. 14. Results on $A_{UL}$ for the $\vec{e}\vec{p} \to e\pi^+(n)$ channel as a function of azimuthal angle $\phi^*$, integrated over $\cos\theta^* = (0.5,1.0)$, for six $Q^2$ bins and three $W$ bins. From top to bottom the six $Q^2$ bins are as follows: $Q^2 = (0.0187,0.0317)$ [1.3 $NH_3$ long target for $W = (1.12,1.34)$ and $(1.34,1.58)$ GeV/$c^2$, and 2.0 $NH_3$ long top target for $W = (1.58,1.82)$ GeV/$c^2$]; (0.156,0.266) and (0.266,0.452) (GeV/$c$)$^2$ (2.0 GeV $NH_3$ long top target); (0.0919,0.156),(0.156,0.266), and (0.266,0.452) (GeV/$c$)$^2$ (3.0 GeV $NH_3$ long top target); from left to right the $W$ bins are as follows: $W = (1.12,1.34),(1.34,1.58),(1.58,1.82)$ GeV/$c^2$. In each panel, the horizontal scale is from 0° to 360° in $\phi^*$ and the vertical scale is from −1 to 1. Data are compared to four calculations: MAID2007 (solid) [13], JANR (dashed) [14], SAID (dash-dotted) [15], and DMT2001 (dotted) [16].

The method of integrating the data for the combined bins was built upon the acceptance correction described in Sec. III H: To correct for the acceptance, each event in the asymmetry bin was divided by the acceptance of that particular event, then summed to be used as $N_{\uparrow\Uparrow,\uparrow\Downarrow,\downarrow\Uparrow,\downarrow\Downarrow}$ in Eqs. (37)–(39). To integrate from asymmetry bins into combined bins, these acceptance-corrected $N_{\uparrow\Uparrow,\uparrow\Downarrow,\downarrow\Uparrow,\downarrow\Downarrow}$ from each asymmetry bin was summed, and used as the combined $N_{\uparrow\Uparrow,\uparrow\Downarrow,\downarrow\Uparrow,\downarrow\Downarrow}$ to evaluate the asymmetries for the combined bin. Using this method, the integrated asymmetries are direct reflections of the ratio of the physical cross sections integrated over the combined bin except for regions that had zero acceptance. To compare with theory, we calculated the cross sections $\sigma_{t,et,0}$ for each asymmetry bin, then summed the calculated cross sections over combined bins except for asymmetry bins where there was no data (zero acceptance).

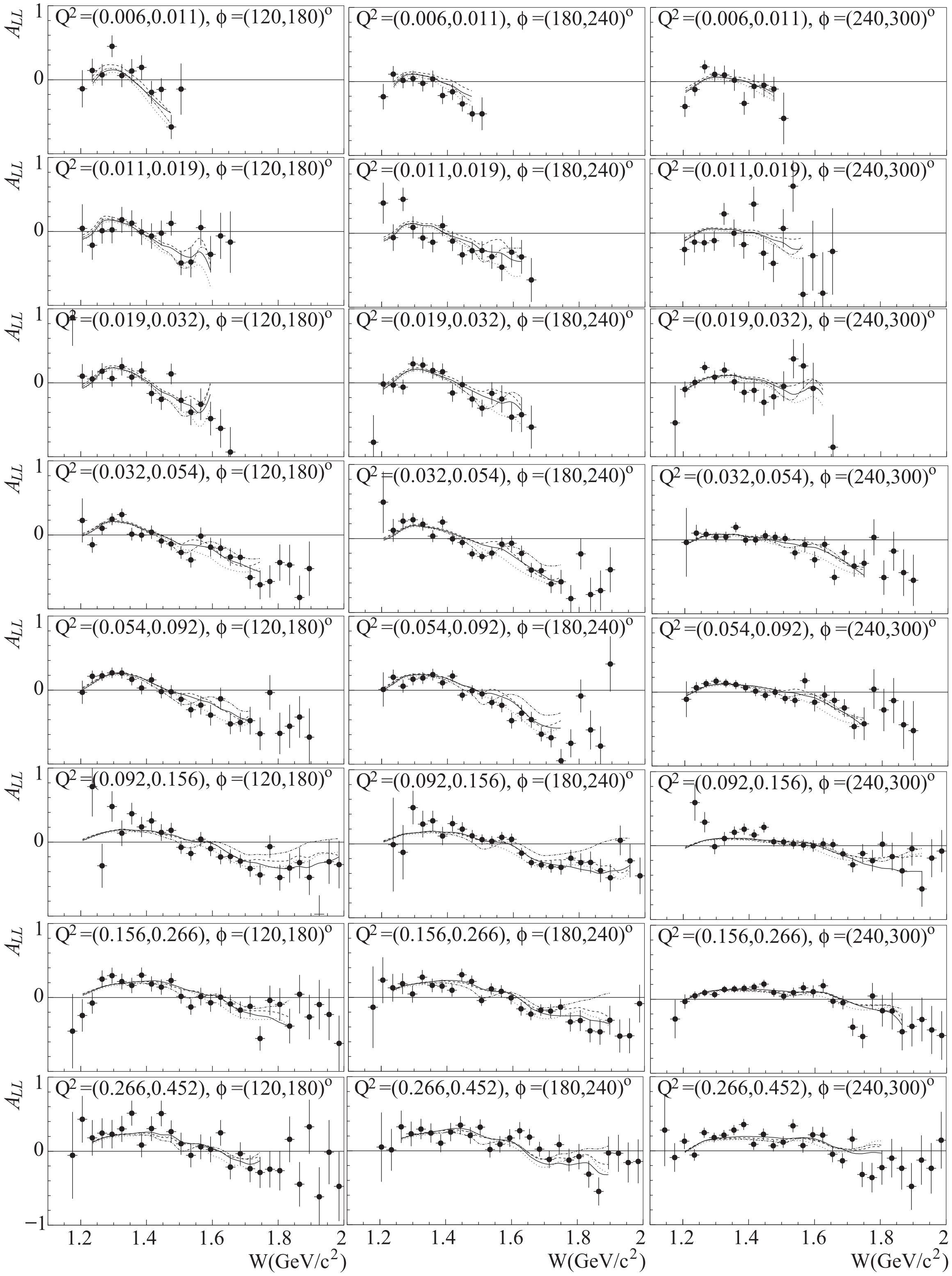

FIG. 15. Results on the double-spin symmetries $A_{LL}$ for the $\vec{e}\vec{p} \to e\pi^+(n)$ channel as a function of the invariant mass $W$ in GeV/$c^2$, integrated over $\cos\theta^* = (0.5,1.0)$, for increasing $Q^2$ ranges and three 60° $\phi^*$ bins. From top to bottom the $Q^2$ bins are (0.00646,0.011) and (0.011,0.0187) (1.1 GeV NH$_3$ long bottom target), (0.0187,0.0317) and (0.0317,0.054) (1.3 GeV NH$_3$ long top target), (0.054,0.0919) (2.0 GeV NH$_3$ long top target), (0.0919,0.156),(0.156,0.266), and (0.266,0.452) (GeV/$c$)$^2$ (3.0 GeV NH$_3$ long top target). From left to right the $\phi^*$ bins are $\phi^* = (120°,180°)$,$(180°,240°)$, and $(240°,300°)$. In each panel, the horizontal scale is from 1.1 to 2 GeV/$c^2$ in $W$ and the vertical scale is from −1 to 1. Data are compared to four calculations: MAID2007 (solid) [13], JANR (dashed) [14], SAID (dash-dotted) [15], and DMT2001 (dotted) [16].

The ratio of the summed cross sections [Eqs. (20) and (21)] was taken as the calculated asymmetry for the combined bin. In the following we will present some representative results.

### A. Results on target asymmetry $A_{UL}$

Figure 13 shows, in increasing $Q^2$ ranges, the $A_{UL}$ results as a function of $W$ for three $\phi^*$ bins $(120^\circ,180^\circ),(180^\circ,240^\circ),(240^\circ,300^\circ)$, and integrated over $0.5 < \cos\theta^* < 1.0$. Results for the $\phi^* = (0^\circ,60^\circ)$ and $(300^\circ,360^\circ)$ have less statistics and are not shown. Results for the $\phi^* = (60^\circ,120^\circ)$ bin have comparable statistics as Fig. 13 but are not shown here for brevity. In general, we see that the agreement between these $A_{UL}$ results and the four calculations, MAID2007 (solid) [13], JANR (dashed) [14], SAID (dash-dotted) [15], and DMT2001 (dotted) [16], is very good in the $W < 1.5$ (GeV/$c^2$) region, but for the region $1.5 < W < 1.8$ (GeV/$c^2$), all four calculations differ from each other and none agrees well with data, although the MAID2007 curve (solid) approximates the data better than the other three.

To study these results further for different $W$ regions, we show in Fig. 14 $A_{UL}$ results as a function of $\phi^*$ for three $W$ ranges and between $Q^2 = 0.0187$ and 0.452 (GeV/$c$)$^2$. Results for lower $Q^2$ ranges, down to 0.00646 (GeV/$c$)$^2$, are available from the 1.1-GeV data but only cover $1.2 < W < 1.5$ (GeV/$c^2$) and thus are not presented here. From Fig. 14, for the lower two $W$ bins (1.12,1.34) and (1.34,1.58) GeV/$c^2$, the four calculations provide similar predictions and all agree with data. But for the $W = (1.58,1.82)$ GeV/$c^2$ region, only the MAID2007 (solid) and the DMT2001 (dotted) calculations provide the correct sign, and MAID2007 approximates the data better than the other three although it does not agree with data perfectly. It is clear that all four calculations can be improved in the $W > 1.58$ GeV/$c^2$ region throughout the $Q^2$ range shown.

### B. Results on the double-spin asymmetry $A_{LL}$

Figure 15 shows the double-spin asymmetry $A_{LL}$ results as a function of $W$ for eight $Q^2$ bins, three $\phi^*$ bins, and integrated over $\cos\theta^* = (0.5,1.0)$. These results are compared with four calculations: MAID2007 (solid) [13], JANR (dashed) [14], SAID (dash-dotted) [15], and DMT2001 (dotted) [16]. Note that our definition for $A_{LL}$ has the opposite sign from theories; see Sec. I A. Results for the $\phi^* = (0^\circ,60^\circ)$ and $(300^\circ,360^\circ)$ bins have less statistics and are not shown. Results for the $\phi^* = (60^\circ,120^\circ)$ bin have comparable statistics as Fig. 13 but are not shown here for brevity. Overall the data agree very well with all four calculations. For all $\phi^*$ bins, the sign of $A_{LL}$ in the region of the $N(1520)3/2^-$ and the $N(1680)5/2^+$ is positive in the high $Q^2$, but start to cross or approach zero in the lower $Q^2$ bin, within (0.0919,0.156) (GeV/$c$)$^2$ for $N(1520)3/2^-$ and within $Q^2 = (0.266,0.452)$ (GeV/$c$)$^2$ for $N(1680)5/2^+$, respectively. This is in agreement with the suggestion in Sec. I that $A_{LL}$ turns to positive at high $Q^2$ values from helicity conservation, but may become negative near the real photon point.

## V. SUMMARY

We present here data on the target and double-spin asymmetry $A_{UL}$ and $A_{LL}$ on the $\vec{e}\vec{p} \to e\pi^+(n)$ channel using data taken on a polarized NH$_3$ target, from the EG4 experiment using CLAS in Hall B of Jefferson Lab. These data have reached a low $Q^2$ region from 0.0065 to 0.35 (GeV/$c$)$^2$ that was not accessed previously. They suggest a transition in $A_{LL}$ from positive at higher $Q^2$ to negative values below $Q^2 \approx 0.1$ (GeV/$c$)$^2$ in the region $1.5 < W < 1.7$ GeV/$c^2$, in agreement with both previous data from CLAS (high $Q^2$) [20,22] and the real photon data at $Q^2 = 0$. Our results show that while all model calculations agree well with $A_{LL}$, in general there is room for improvements for $A_{UL}$ in the high-mass resonance region $W > 1.58$ GeV/$c^2$ where predications from various models differ significantly.

## ACKNOWLEDGMENTS

The authors gratefully acknowledge the work of Jefferson Lab staff in the Accelerator and Physics Divisions that resulted in the successful completion of the experiment. This work was supported by the U.S. Department of Energy (DOE), the U.S. National Science Foundation, the U.S. Jeffress Memorial Trust, the United Kingdom's Science and Technology Facilities Council (STFC) under Grants No. ST/L005719/1 and No. GR/T08708/01, the Italian Istituto Nazionale di Fisica Nucleare, the French Institut National de Physique Nucléaire et de Physique des Particules, the French Centre National de la Recherche Scientifique, and the National Research Foundation of Korea. This material is based upon work supported by the U.S. Department of Energy, Office of Science, Office of Nuclear Physics under Contract No. DE-AC05-06OR23177.

---

[1] D. J. Gross and F. Wilczek, Phys. Rev. Lett. **30**, 1343 (1973).
[2] H. D. Politzer, Phys. Rev. Lett. **30**, 1346 (1973).
[3] V. D. Burkert and T. S. H. Lee, Int. J. Mod. Phys. E **13**, 1035 (2004).
[4] I. G. Aznauryan and V. D. Burkert, Prog. Part. Nucl. Phys. **67**, 1 (2012).
[5] C. Hoelbling, Acta Phys. Pol. B **45**, 2143 (2014).
[6] A. Ukawa, J. Stat. Phys. **160**, 1081 (2015).
[7] V. Bernard, N. Kaiser, T. S. H. Lee, and U. G. H. Meissner, Phys. Rept. **246**, 315 (1994).
[8] V. Bernard, N. Kaiser, and U. G. Meissner, Nucl. Phys. A **607**, 379 (1996); **633**, 695 (1998).
[9] X. Zheng *et al.* (Jefferson Lab Hall A Collaboration), Phys. Rev. Lett. **92**, 012004 (2004).
[10] X. Zheng *et al.* (Jefferson Lab Hall A Collaboration), Phys. Rev. C **70**, 065207 (2004).
[11] M. Warns, W. Pfeil, and H. Rollnik, Phys. Rev. D **42**, 2215 (1990).
[12] V. D. Burkert, R. De Vita, M. Battaglieri, M. Ripani, and V. Mokeev, Phys. Rev. C **67**, 035204 (2003).
[13] D. Drechsel, S. S. Kamalov, and L. Tiator, Eur. Phys. J. A **34**, 69 (2007).
[14] I. G. Aznauryan *et al.* (CLAS Collaboration), Phys. Rev. C **80**, 055203 (2009).

[15] The SAID partial wave analysis, R. A. Arndt *et al.*, [http://gwdac.phys.gwu.edu/]; R. A. Arndt, W. J. Briscoe, M. W. Paris, I. I. Strakovsky, and R. L. Workman, Chin. Phys. C **33**, 1063 (2009).

[16] S. S. Kamalov and S. N. Yang, Phys. Rev. Lett. **83**, 4494 (1999).

[17] R. De Vita *et al.* (CLAS Collaboration), Phys. Rev. Lett. **88**, 082001 (2002); **88**, 189903 (2002).

[18] R. De Vita (CLAS Collaboration), Nucl. Phys. A **699**, 128 (2002).

[19] A. Biselli *et al.* (CLAS Collaboration), Phys. Rev. C **68**, 035202 (2003).

[20] J. Pierce, Ph.D thesis, University of Virginia, 2008.

[21] S. Careccia, Ph.D thesis, Old Dominion University, 2012.

[22] P. E. Bosted *et al.* (CLAS Collaboration), arXiv:1604.4350.

[23] D. E. Groom *et al.* (Particle Data Group), Eur. Phys. J. C **15**, 1 (2000).

[24] S. Capstick, Phys. Rev. D **46**, 2864 (1992).

[25] M. Gottschall *et al.* (CBELSA/TAPS Collaboration), Phys. Rev. Lett. **112**, 012003 (2014).

[26] H. Iwamoto (CLAS Collaboration), AIP Conf. Proc. **1432**, 275 (2012).

[27] D. Schott *et al.* (CLAS Collaboration), AIP Conf. Proc. **1735**, 030016 (2016).

[28] D. I. Sober, M. Khandaker, and D. G. Crabb, *Helicity Structure of Pion Photoproduction*, JLab CLAS Experiment 04-102 (Thomas Jefferson National Accelerator Facility, Newport News, 2004).

[29] M. Battaglieri, R. De Vita, A. Deur, and M. Ripani, *The GDH Sum Rule with Nearly Real Photons and the Proton $g_1$ Structure Function at Low Momentum Transfer*, JLab CLAS Experiment 03-006 (Thomas Jefferson National Accelerator Facility, Newport News, 2003).

[30] A. Deur, G. Dodge, and K. Slifer, *Measurement of the Gerasimov-Drell-Hearn Integral at Low $Q^2$ on the Neutron and Deuteron*, JLab Proposal 05-111 (Thomas Jefferson National Accelerator Facility, Newport News, 2005).

[31] S. B. Gerasimov, Sov. J. Nucl. Phys. **2**, 430 (1966) [Yad. Fiz. **2**, 598 (1965)].

[32] S. D. Drell and A. C. Hearn, Phys. Rev. Lett. **16**, 908 (1966).

[33] M. Anselmino, B. L. Ioffe, and E. Leader, Sov. J. Nucl. Phys. **49**, 136 (1989) [Yad. Fiz. **49**, 214 (1989)].

[34] X. Ji, C. W. Kao, and J. Osborne, Nucl. Phys. A **684**, 363 (2001).

[35] Hyekoo Kang, *Measurement of the Proton Spin Structure Functions at Very Low Momentum Transfer* (Seoul National University, Seoul, 2015).

[36] B. A. Mecking *et al.* (CLAS Collaboration), Nucl. Instrum. Meth. A **503**, 513 (2003).

[37] G. Adams *et al.*, Nucl. Instrum. Meth. A **465**, 414 (2001).

[38] E. Cisbani *et al.*, Nucl. Instrum. Meth. A **496**, 305 (2003).

[39] D. G. Crabb and D. B. Day, Nucl. Instrum. Meth. A **356**, 9 (1995).

[40] C. D. Keith *et al.*, Nucl. Instrum. Meth. A **501**, 327 (2003).

[41] J. S. Price *et al.*, in *Proceedings of the 12th International Symposium on High-Energy Spin Physics, SPIN 96, Amsterdam, Netherlands, 1996* (World Scientific, Singapore, 1997), p. 727.

[42] J. S. Price *et al.*, in *Proceedings of the 7th International Workshop on Polarized Gas Targets and Polarized Beams, Urbana, IL, USA* (1997), pp. 446-450.

[43] J. S. Price *et al.*, in *Proceedings of the 13th International Symposium on High-Energy Spin Physics, SPIN'98, Protvino, Russia, 1998* (World Scientific, Singapore, 1999), p. 554.

[44] M. Steigerwald, [http://www.jlab.org/accel/inj_group/mott/mott.pdf].

[45] K. Joo *et al.* (CLAS Collaboration), Phys. Rev. C **70**, 042201 (2004).

[46] K. Park *et al.* (CLAS Collaboration), Phys. Rev. C **77**, 015208 (2008).

[47] K. Adhikari, Ph.D thesis, Old Dominion University, 2013.

[48] A. Klimenko and S. Kuhn, Momentum Corrections for E6, CLAS-NOTE 2003-005 [http://www.jlab.org/Hall-B/notes/clas_notes03/03-005.pdf].

[49] J. Beringer *et al.* (Particle Data Group), Phys. Rev. D **86**, 010001 (2012).

[50] P. E. Bosted, Phys. Rev. C **51**, 409 (1995).

[51] R. De Vita, Ph.D thesis, Università di Genova, 2000.

[52] B. Adeva *et al.* (Spin Muon Collaboration), Nucl. Instrum. Meth. A **419**, 60 (1998).

[53] K. Abe *et al.* (E143 Collaboration), Phys. Rev. D **58**, 112003 (1998).

[54] O. A. Rondon, Phys. Rev. C **60**, 035201 (1999).

[55] A. Afanasev, I. Akushevich, V. Burkert, and K. Joo, Phys. Rev. D **66**, 074004 (2002); J. Gilfoyle *et al.*, [http://www.richmond.edu/∼ggilfoyl/research/RC/wvo.html].